International Journal of Biological Macromolecules 330 (2025) 147763

Contents lists available at ScienceDirect

International Journal of Biological Macromolecules

journal homepage: www.elsevier.com/locate/ijbiomac

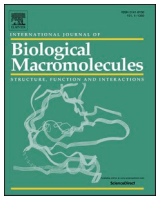

Porous chitin nanofibers combined with adipose-derived stem cells promote diabetic wound healing via PPAR-γ activation

Ziyang Zhang [a,1], Yaoyi Zheng [a,1], Ziyi Wang [a], Yi Li [a], Yunen Liu [b,*], Zhonghua Luo [b,*]

[a] Graduate School, Shenyang Medical College, No. 146, Huanghe North Street, Shenyang 110034, China
[b] School of Shuren International, School of Innovation and Entrepreneurship, Liaoning Provincial Key Laboratory of Skin, Mucosa and Soft Tissue Trauma Repair and Reconstruction, Shenyang Medical College, No. 146, Huanghe North Street, Shenyang, 110034, China

ARTICLE INFO

Keywords:
Chitin nanofibers
Adipose stem cells
Diabetic wound
Proteomics
PPAR signaling pathway

ABSTRACT

Chronic wounds of diabetes are one of the serious complications that cause disability or death in patients with diabetes, posing a significant clinical challenge. Therefore, porous chitin nanofibers (CR) were prepared from silk and squid cartilage, and combined with adipose-derived stem cells (ADSCs) transplantation to promote wound healing in type 2 diabetes mellitus (T2DM) in this study. The results of scanning electron microscopy (SEM), fourier transform infrared spectroscopy (FTIR), and X-ray diffraction (XRD) indicated that the CR had an obvious three-dimensional porous structure. The in vivo and in vitro degradation experiments showed that the CR had good degradability. The live/dead staining and hemolysis experiments demonstrated that the CR had good biocompatibility. The results of in vivo experiments indicated the results of H&E staining and masson staining indicated that the CR combined with the ADSCs transplantation significantly accelerated the wound healing of T2DM mice. Immunohistochemical staining indicated that the CR combined with the ADSCs transplantation significantly increased collagen deposition and cell proliferation, and regulated macrophage expression. In addition, the CR combined with the ADSCs transplantation can increase the expression of α-SMA and VEGF-A to promote angiogenesis. Proteomics sequencing and western blotting experiments revealed that the CR combined with the ADSCs transplantation accelerated wound healing by activating the PPAR-γ signaling pathway to regulate the expressions of MMP-1, SCD-1 and ACOX-2. To sum up, all these results suggested that the CR combined with the ADSCs transplantation could provide a promising method for wound healing in T2DM.

1. Introduction

Diabetic patients are in a state of hyperglycemia for a long time, which is prone to various complications, among which the difficulty of wound healing is a common and serious problem [1,2]. Hyperglycemia can affect the normal metabolic process of the body. The main causes involve microvascular lesions, oxidative stress, nerve damage, ultimately leading to a significant decrease in wound healing ability [3,4], and seriously reducing the quality of life of diabetic patients. At present, the conventional treatment methods for diabetic wounds include blood sugar control, debridement and anti-infection. However, there are many problems at the same time, such as long treatment time, unstable therapeutic effect and high medical and health care costs [5,6]. Meanwhile, the application of traditional wound dressings cannot provide a favorable environment for tissue regeneration [7]. Therefore, seeking effective treatment methods to promote the healing of diabetic wounds has become an important research topic in the fields of clinical medicine and regenerative medicine.

Multiple studies have shown that stem cell transplantation therapy is a promising medical field, offering new possibilities for treating various complex wounds [8]. Adipose-derived stem cells (ADSCs), as a type of stem cell with the potential for self-renewal and multi-directional differentiation, have demonstrated great potential for wound repair [9]. It can differentiate into various cell types, including keratinocytes, endothelial cells, fibroblasts. These key cells are involved in all stages of wound repair [10]. In addition, the ADSCs can secrete a variety of growth factors, such as fibroblast Growth Factor, FGF), VEGF and epidermal Growth Factor (EGF), which can help the wound tissue to regenerate and repair [11,12]. The ADSCs, with their unique biological functions and high safety, have been widely applied in the treatment of

* Corresponding authors.
E-mail addresses: liuye990116@163.com (Y. Liu), zhonghua_2398@163.com (Z. Luo).
[1] These authors contributed equally to this work.

https://doi.org/10.1016/j.ijbiomac.2025.147763
Received 27 May 2025; Received in revised form 31 July 2025; Accepted 16 September 2025
Available online 19 September 2025

various types of wounds. However, the microenvironment of high glucose, high oxidative stress and high bacterial load in diabetic wounds significantly reduces the survival rate and function of ADSCs, limiting the clinical efficacy of cell therapy alone [13].

To overcome the key challenge of survival and functional limitations of ADSCs in the harsh microenvironment of diabetes, researchers are actively seeking strategies to enhance their efficacy by constructing suitable microenvironments through biomaterials. In recent years, the development of natural multifunctional materials has opened up new ideas for the treatment of diabetic wounds [14,15]. Chitin is a natural high-molecular polysaccharide extracted from the cell walls of crustaceans, insects and fungi. It has attracted much attention due to its excellent biocompatibility and ability to promote cell proliferation and differentiation [16–18]. Meanwhile, the natural anti-inflammatory and antibacterial components contained in chitin can alleviate inflammatory responses and reduce the risk of infection [19–20]. However, the application of a single component in wound dressings may be limited by poor mechanical properties and the lack of porosity. Due to its excellent mechanical properties, the modification of chitin by silk protein can enhance the overall mechanical strength and controllable pore structure of the composite material, making it an ideal material for the healing of diabetic wounds [21,22]. The preparation of porous nanofiber materials allows for gas exchange and secretion absorption, providing the necessary space for cell growth and angiogenesis [23,24], while also effectively blocking the invasion of microorganisms in the external environment. In previous studies, porous nanofiber materials, as an excellent dressing, can be directly applied to the wound surface or used in combination with stem cells, growth factors, antibacterial drugs to synergistically improve the efficiency of wound healing [25,26]. These materials have broad application prospects in clinical treatment, especially showing great potential in dealing with refractory wounds such as chronic wounds, burns and diabetic foot ulcers. However, the synergistic effect and specific mechanism of action of porous nanofiber materials combined with the ADSCs transplantation in diabetic wounds remain unclear, especially in the key links of regulating inflammation regression and tissue remodeling, which lack in-depth research.

Based on this, the effect of the CR combined with the ADSCs transplantation in promoting the healing of diabetic wounds was explored (Scheme 1). The chemical structure and crystallization characteristics of the CR were characterized by fourier transform infrared spectroscopy (FTIR) and X-ray diffraction (XRD). The microstructure of the CR was observed by scanning electron microscope (SEM). The degradation ability of the CR was evaluated through in vivo and in vitro degradation experiments. The cytocompatibility of the CR was evaluated using the Calcein-AM/PI live and dead staining kit and the cell counting kit-8 (CCK-8). The hemolysis test was conducted to calculate the hemolysis rate to evaluate the blood compatibility of the CR. In the vivo experiment, a wound model of type 2 diabetes mellitus (T2DM) was established to study the healing effect of the CR combined with the ADSCs transplantation on the wound. Proteomic methods were used to analyze the activation of the PPAR-γ pathway by CR combined with ADSCs transplantation, which synergistically regulates the local inflammatory microenvironment of diabetic wounds, promotes angiogenesis and ordered collagen deposition, thereby accelerating wound healing. This study provides a novel biomaterial - cell composite strategy and theoretical basis for the treatment of diabetic wounds.

2. Materials and methods

2.1. Material

The squid cartilage and silk were provided by Guangdong Jihua Laboratory. The 10 % Fetal Bovine Serum (FBS, 164210–500) was purchased from Wuhan Pricella Biotechnology Co., Ltd. The Calcein AM/PI dual staining kit (CA1630), Masson's Trichrome Stain Kit (G1340) and Collagenase Type I (C8140) were purchased from Beijing

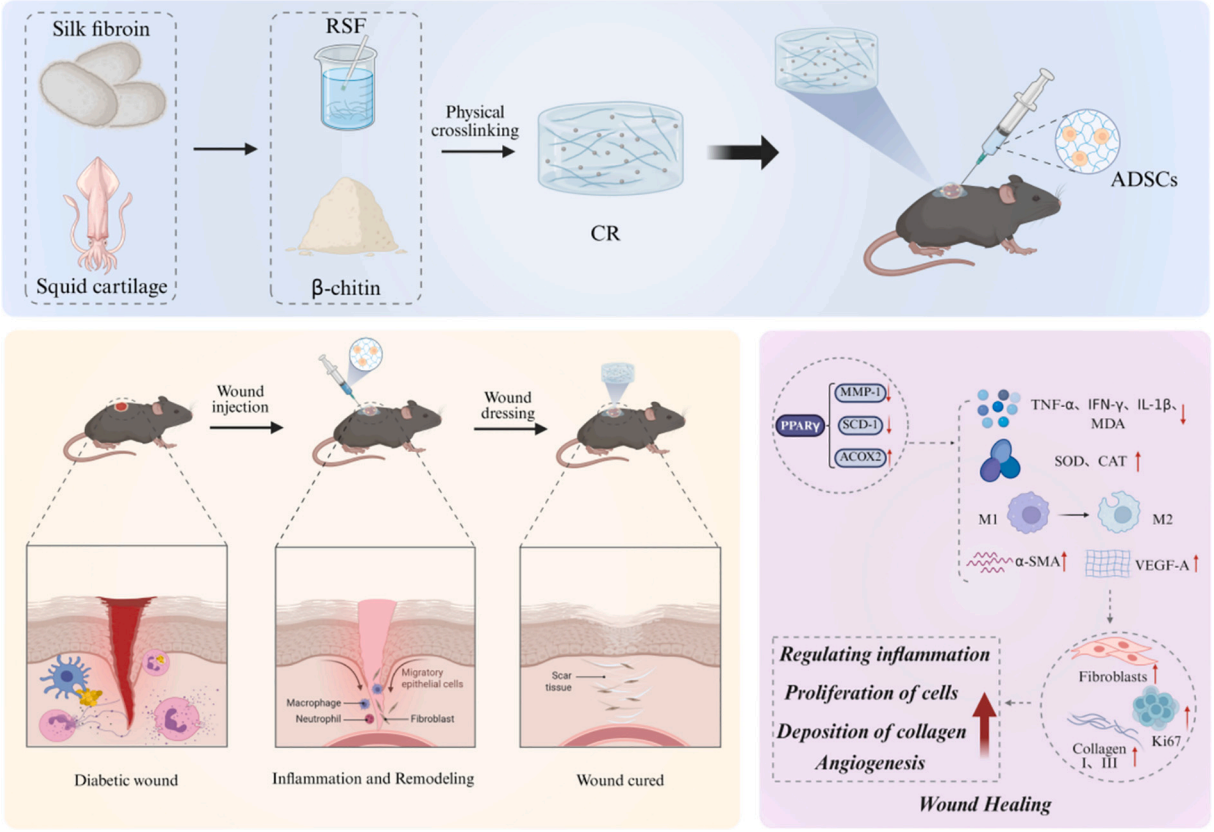

Scheme 1. Mechanism diagram of porous chitin nanofibers combined with adipose-derived stem cells transplantation in promoting wound healing of T2DM.

Solarbio Technology Co. The cell counting kit-8 (CCK-8, C0038) was purchased from Beijing Beyotime Biotech Inc. The Mammalian Protein Extraction Kit (FD0889) and BCA protein assay Kit (FD2001) were bought from Fdbio Science Biotech Co., Ltd. The Ki67 (ab15580), PPAR-γ (ab209350), ACOX2 (ab197808), and SCD-1 (ab236868) were purchased from Abcam Trading Co. Both CD86 (ab234000) and CD163 (ab189915) were purchased from Abcam, USA. The Collagen Type I (14695–1-AP), Collagen Type III (22734–1-AP), α-SMA (14395–1-AP), VEGF-A (66828–1-Ig) and MMP-1 (10371–2-AP) were purchased from Proteintech Biotech. ADSCs (HUM-CYY-a009) were purchased from Xi 'an Chuyunyuan Medical Technology Co., LTD. Fibroblasts (L929, CL-0137) were provided by Wuhan Ponosi Life Technology Co., Ltd.

2.2. Preparation of the recombinant silk fibroin (RSF), the chitin nanofibers (CNF) and the CR

10 g of silk was placed in a 0.5 % sodium bicarbonate aqueous solution to remove sericin protein. After drying, it was dissolved in a LiBr aqueous solution and concentrated in a 15 % PEG-20000 solution. Eventually, a 10 % the RSF solution was obtained. The squid cartilage was respectively placed in 4 % sodium hydroxide solution and 2 % hydrochloric acid solution for deproteinization and inorganic salt removal treatment to obtain purified β -chitin. 0.2 g of purified β -chitin was dispersed in 100 mL of deionized water and crushed to obtain the CNF with a concentration of 0.2 %. Then, the concentrated silk fibroin aqueous solution was diluted to 4 % with deionized water, and the CNF was added. 300 U/mL horseradish peroxidase and 0.5 % (*v*/v) hydrogen peroxide were added to the above mixed solution, and it was left to stand and cross-link at room temperature to obtain the CR.

2.3. Characterization of the RSF, the CNF and the CR

2.3.1. Infrared spectroscopy (FTIR)

The chemical composition and structural characteristics of the samples were analyzed by Nicolet 6700 Fourier Transform Infrared Spectrometer (FT-IR, Thermo Fisher, USA). The samples were tested in the transmission mode, with the resolution and scanning range set at 4 cm^{-1} and 4000–550 cm^{-1} respectively.

2.3.2. X-ray diffraction (XRD)

The crystal structure of the sample was analyzed using the Rigaku SmartLab SE X-ray diffractometer (XRD, Science, Japan). The scanning speed and scanning range were set to 4°/min and 5–70° respectively.

2.3.3. Scanning Electron microscope (SEM)

The morphology of the sample was observed by S4800 field emission scanning electron microscope (FE-SEM, Hitachi, Japan). After freeze-drying the samples, they were sliced and gold-plated, then fixed on the conductive sample stage. The SEM was used for observation and photography. Pore size was conducted on at least five SEM images from different fields of view through ImageJ.

2.3.4. Porosity test

CR and CNF were cut into regular shapes and then freeze-dried, and the drying mass was called m1, and the volume of the sample was measured as V. Subsequently, CR and CNF were completely immersed in anhydrous ethanol, and a vacuum pump was connected for 1 h to ensure that ethanol fully penetrated into the pore structure of the sample. After the completion, the sample was taken out and the residual ethanol on the surface was wiped off, and then the mass m2 of the sample soaked in ethanol was weighed. Porosity was calculated according to the following formula.

$$\text{Porosity}\ (\%) = \frac{m_2 - m_1}{\rho_{ethanol} \times V} \times 100$$

2.3.5. In vitro degradation test

The in vitro degradation of the samples was analyzed using collagenase I. The initial weight of the sample was W_0. Next, it was mixed with 2 U/mL collagenase solution and the reaction was carried out under constant temperature shaking at 37 °C. At different time periods, the samples were taken out and the surface moisture was removed with filter paper. The weight of the samples was measured as W_t. The degradation rate is calculated by the following formula.

$$\text{In vitro degradation rate}\ (\%) = \frac{W_t}{W_0}$$

Among them, W_0 was the initial weight of the sample, and W_t was the weight of the sample at different time points.

2.3.6. In vivo degradation test

The Male SD rats, weighing 200 ± 10 g and aged 6–8 weeks, were provided by Beijing Huafukang Biotechnology Co., LTD. The animal experiment protocol of this study has been reviewed and approved by the Ethics Committee of Shenyang Medical College (No. SYYXY2023030501). The Rats were anesthetized with isoflurane, and the rat back implantation model was established to evaluate the in vivo degradation of the CR. On the 7th and 14th days, the rats were anesthetized. The tissues around the samples were fixed in 10 % formalin fixative, paraffin sections were made, and the histopathological changes were evaluated by HE staining.

2.4. Biocompatibility evaluation

2.4.1. Staining of live/dead cells

L929 cells were inoculated into 6-well plates at a density of 5×10^5 cells per well and cultured until adherent. 2 mL of the extract solutions of different groups of materials were used instead of the culture medium for continued culture for 24 h and 48 h. Adherent cells were collected and resuspended in Assay Buffer to make the cell count at 1×10^6 cells/mL. For every 1 mL of cells, 2 μL of Calcein-AM staining solution (stained at 37 °C in the dark for 25 min) and 5 μL of PI staining solution (stained at room temperature in the dark for 5 min) were added successively to stain the cells. Finally, the cells were observed under a fluorescence microscope.

2.4.2. Cytotoxicity test

L929 cells were inoculated in 96-well plates at a density of 5×10^4 cells per well and cultured for 24 h. Afterwards, 100 μL of the RSF, the CNF and the CR extracts were respectively used to replace the culture medium for continued culture for 24 h, while the control group was replaced with normal culture medium. 100 μL of 10 % CCK-8 solution was added to each well respectively and incubated at 37 °C for 4 h. Then, the absorbance of the solution was determined at 450 nm using an enzyme-linked immunosorbent assay reader. The cell activity was calculated using the following formula.

$$\text{Cell viability}\ (\%) = \frac{A_{sample} - A_{blank}}{A_{control} - A_{blank}}$$

Among them, A_{sample} represents the absorbance of the cells after adding the sample, $A_{control}$ represents the absorbance containing only the cells, and A_{blank} represents the absorbance containing only the culture medium.

2.4.3. Blood compatibility test

The whole blood of anticoagulant rats was collected and centrifuged for 15 min. After the supernatant was discarded, it was washed with PBS until colorless. The experimental groups were respectively added with 1 mL of 2 % blood cell suspension containing 20 μg of nanomaterials. The positive control group and the negative control group were respectively added with 1 mL of 2 % blood cell suspension diluted with ultrapure water and PBS. After incubation at 37 °C for 4 h, the samples were

centrifuged at 3000 rpm for 15 min and photographed. The supernatant was aspirated and the absorbance was measured at 540 nm. The following formulas were used to calculate the hemolysis rate.

$$\text{Hemolysis rate } (\%) = \frac{A_{sample} - A_{PBS}}{A_{ddH2O} - A_{PBS}}$$

Among them, A_{sample}, A_{PBS} and A_{ddH2O} were the absorbance values of the experimental group, the negative control group and the positive control group, respectively.

2.4.4. Test of the binding rate of the CR to TNF-α and IFN-γ

The concentration changes of TNF-α and IFN-γ proteins before and after incubation with the gel were detected by ELISA kits to explore the ability of the hydrogel to capture them. The samples from the RSF group, the CNF group and the CR group were placed in 48-well plates, with three parallel samples in each group. TNF-α protein and IFN-γ protein solutions were added and incubated at room temperature with each group of samples. Meanwhile, a pure protein control group was set up. The supernatant was collected 24 h later and quantitatively detected using an ELISA kit.

2.5. Identification of ADSCs surface marker proteins by flow cytometry

The third-generation ADSCs were digested with trypsin and the cell precipitates were collected by centrifugation. The precipitates were resuspended in a staining buffer containing antibodies PE-CD73 (bsm-30,125 M-PE, Bioss, China)、APC-CD105 (FBA10971A, RD, China)、PE-Cy7-CD34 (BF00619, RD, China)、PerCP-HLA-DR (FBA4869C, RD, China) for detecting surface markers of mesenchymal stem cells and incubated at 4 °C in the dark for 30 min. After washing with PBS, the expressions of CD73, CD105, CD34 and HLA-DR were detected using the FACSCalibur (BD Biosciences) flow cytometer. The data were analyzed using FlowJo V10 software.

2.6. Establishment and sampling of wound models in type 2 diabetic mice

The 60 SPF-grade male C57BL/6 J mice (6–8 weeks old, body weight range 22 ± 2 g) used in the experiment were from Beijing Huafukang Biotechnology Co., LTD. The animal experiment protocol of this study has been reviewed and approved by the Ethics Committee of Shenyang Medical College (No. SYYXY2023030501). The mice in the control group ($n = 8$) were fed with normal feed, while the mice in the model group ($n = 52$) were fed with a high-fat diet (HFD). After 6 weeks, the model mice were intraperitoneally injected with 50 mg/kg streptozotocin (STZ) for 3 consecutive days. The fasting blood glucose (FBG) values of mice were measured at 72 h and 1 week after the injection of STZ, respectively. When the FBG values all exceeded 11.1 mmol/L, it indicated that the modeling of T2DM mice was successful. The mice were removed due to unsuccessful modeling, the successfully modeled mice were randomly divided into the T2DM group, the ADSCs group, the CR group, and the ADSCs+CR group, with 8 mice in each group [27]. Afterwards, the mice were anesthetized with isoflurane, and an 8 mm wound was induced in the middle of the lumbar vertebrae with scissors. The control group and the T2DM group received no treatment. The ADSCs (the injection dose was 1×10^6, 200 μL) were injected at multiple points around the wound surface, it will be conducted on days 0, 1 and 2. While the CR was placed on the wound surface and replaced at 0,3,6 and 9 days respectively. The body weight and fasting blood glucose levels of the mice were monitored weekly. During the experiment, photos of the wound closure of mice were taken, and the skin around the wound was collected at the corresponding time points for subsequent experiments. The wound healing rate was calculated through the following formula.

$$\text{Wound closure rate } (\%) = \frac{A_0 - A_t}{A_0}$$

Among them, A_0 was the initial wound area, and A_t was the wound area at a certain time point (days 0, 5, 9, and 13) [28].

2.7. Histopathological analysis

2.7.1. H&E staining and Masson staining

The skin tissues of mice on the 7th day were fixed with 4 % paraformaldehyde, then subjected to ethanol gradient dehydration and paraffin embedding, and the embedded blocks were cut into sections 5 μm thick. According to the plan in the instruction manual, hematoxylin-eosin staining (H&E) and masson staining were performed on the sections, and then they were observed under an optical microscope. The ImageJ software was used to analyze the proportion of collagen fiber area and calculate the volume fraction of collagen fibers in each group.

Collagen volume fraction (%) = blue area with positive collagen/total tissue area ×100 %.

2.7.2. Immunohistochemical analysis

After antigen repair, peroxidase inactivation, and blocking of the slices, primary antibodies (Ki67, 1:1000. Collagen I, 1:1000. Collagen III, 1:1000. CD86, 1:500. CD163, 1:500) were added to the slices and incubated overnight at 4 °C. Then, HRP labeled secondary antibody was added to the slice and incubated at room temperature for 30 min. The sections were colored using diaminobenzidine (DAB), and the cell nuclei were stained with hematoxylin. Finally, the stained sections were captured using a microscope and analyzed with Image J software.

2.7.3. Immunofluorescence analysis

For immunofluorescence staining, primary antibodies (α - SMA, 1:1600. VEGF, 1:400) were added to the sections and incubated overnight at 4 °C. Then, fluorescent secondary antibodies (the corresponding secondary antibody for α-SMA was Alexa Fluor® 488 labeled goat anti-rabbit IgG (H&L), and the corresponding secondary antibody for VEGF was Cy3 labeled goat anti-mouse IgG (H&L), with a dilution ratio of 1:500 for both) were added and incubated at room temperature in the dark for 1 h. After staining was completed, anti-fluorescence attenuation mounting solution (containing DAPI) was added to the tissue sections and they were imaged using confocal microscopy.

2.8. Proteomics sequencing

The wound tissue samples of mice were taken out of a − 80 °C refrigerator. An appropriate amount of the sample was weighed and placed in a mortar pre-cooled with liquid nitrogen, and then thoroughly ground into powder with liquid nitrogen. Samples from each group were respectively added to four times the volume of the powder lysis buffer (1 % Triton X-100, 1 % protease inhibitor) and subjected to ultrasonic lysis. The samples were centrifuged at 12,000 *g* at 4 °C for 10 min. The supernatant was transferred to a new centrifuge tube, and the protein concentration was determined using the BCA kit. Subsequently, the samples were processed through steps such as ethanol precipitation, protein resolubility/reduction/etherification, enzymatic hydrolysis, SDC removal, and peptide desalination, in preparation for subsequent testing. The peptides were dissolved in phase A of the liquid chromatography mobile phase and then separated using the NanoElute ultra-high performance liquid chromatography system. The peptides were labeled using iTRAQ/TMT technology and detected by LC-MS/MS to analyze the spectral information. Bioinformatics analysis was conducted through Hangzhou Jingjie Biotechnology co., LTD. (http://www.ptm-biolab.com.cn), including gene ontology (GO) annotation enrichment analysis, Kyoto Encyclopedia of Genes and genomes (KEGG) annotation enrichment analysis and functional enrichment analysis.

2.9. Western blotting

Tissue proteins were extracted using the mammalian extraction kit and the total protein concentration was determined using the BCA kit.

The samples were separated by sodium dodecyl sulfate - polyacrylamide gel electrophoresis (SDS-PAGE), and the proteins were transferred onto the polyvinylidene fluoride (PVDF) membrane and sealed with 5 % skimmed milk for 1 h. Then, the membrane was incubated with primary antibody (SCD-1, 1:1000. PPAR-γ, 1:1000. MMP-1, 1:1000. ACOX2, 1:1000. GAPDH, 1:1000) at 4 °C overnight. After the membrane was washed, it was incubated with the corresponding secondary antibody. Finally, the strips were visualized using an ECL luminescence meter, and the gray values were calculated using Image J software.

2.10. Statistical analysis

Data were analyzed using GraphPad Prism 9.0 software, and the results were expressed as Mean ± standard deviation (Mean ± SD). Student's *t*-test was used for the comparison between two groups of data, and One-way ANOVA or Multi-way ANOVA was used for the comparison among multiple groups of data. $p < 0.05$ was considered statistically significant.

3. Results

3.1. Preparation and characterization of the CR

The morphologies of the RSF, the CNF suspensions and the CR were shown in Fig. 1A. The RSF and the CNF were prepared from silk and squid cartilage as raw materials, and the CR was finally prepared through physical cross-linking. The microstructure of the CR was observed by SEM, and the results were shown in Fig. 1B-C. It can be seen that the CR was a typical 3D porous structure, the pore size was 106.68 ± 76.99 μm. As shown in Fig. 1D, both CR and CNF exhibited relatively high porosity. Among them, the porosity of CR was 89.1 %, which was higher than that of CNF at 70.6 %. Subsequently, the structure of the prepared CR was characterized by FTIR. It can be known from Fig. 1E that the characteristic peaks of the CNF were at 3435 cm^{-1} and 3265 cm^{-1}, which were attributed to the stretching vibrations of O—H and N—H respectively. In addition, since the molecular chains of β -chitin were arranged in the same direction and the hydrogen bond effect is relatively small, it was a unimodal peak at 1643 cm^{-1}, representing the stretching vibration of C═O (amide I band). After the introduction of the RSF, a characteristic peak of β - chitin amide I band appeared in the CR at 1643 cm^{-1}, and multiple absorption peaks at 1520 cm^{-1} and 1228 cm^{-1} were caused by the overlapping of the stretching vibration absorption peaks of various functional groups. The XRD pattern (Fig. 1F) demonstrated that the two main diffraction peaks of the CR were around 9.0° and 19.5°, respectively, showing wider and more dispersed diffraction peaks, and the main characteristic peaks remain unchanged. The above results suggested that the RSF and the CNF were physically crosslinked.

3.2. The biocompatibility of the RSF, the CNF and the CR

As shown in Fig. 2A, compared with the control group, the RSF group, the CNF group and the CR group all showed a large number of living cells (green) and a small number of dead cells (red). Moreover, compared with 24 h, the number of cells in each group was significantly increased after 48 h, and the morphology was clear, indicating that the cell growth and proliferation status was good. Subsequently, the cell viability of the material was further quantified through the CCK-8 toxicity test. As shown in Fig. 2B, the cell viability of the RSF group, the CNF group and the CR group was all above 90 %. It indicated that the material had no obvious toxicity to cell growth. The appearance images and hemolysis rate statistics of the hemolysis experiment were shown in Fig. 2C-D. The appearance image in Fig. 2C displayed that compared with the ddH_2O positive group, there was no obvious hemolysis in the other groups. Moreover, compared with the ddH_2O positive group, the hemolysis rates of the RSF group, the CNF group and the CR group were 0.88 %, 0.67 % and 0.7 % respectively, all of which were lower than the 5 % hemolysis rate standard stipulated by ISO (Fig. 2D). As shown in Fig. 2E, compared with the RSF and the CNF, the CR group had a higher binding rate of TNF-α, and the clearance rate was about 70 %. Compared with the RSF and the CNF, the CR also showed excellent results in the clearance of IFN-γ, with a clearance rate of about 30 %, as shown in Fig. 2F. The H&E staining on the 7th and 14th days of the in vivo degradation experiment was shown in Fig. 2G. On the 7 th day after operation, there was some inflammatory reaction in the tissues around the CR embedding site, and the CR was gradually degraded. On the 14th day after the operation, the inflammatory response in the CR group was alleviated, and only a small amount of sample residue could be observed. Fig. 2H indicated the in vitro degradation results of the material. The weight of the RSF group and the CR group was slightly increased on the fourth day, and then the weight was gradually decreased. After 43 days, the weight of the RSF group and the CR group was reduced to less than 20 %.

3.3. Identification of ADCSs

As shown in Fig. 3A, CD73 was highly expressed, and its fluorescence intensity was concentrated between 10^4 and 10^5, while the expression level of CD34 was low, and its fluorescence intensity was below 10^3. In Q1 quadrant, the proportion of $CD73^-CD34^+$cells was 37.0 %, while in Q4 quadrant, the proportion of CD73-CD34-double negative cells was 62.6 %. As shown in Fig. 3B, the fluorescence intensity of CD105 was concentrated in the 10^4 interval, and its expression was relatively uniform, while the fluorescence intensity of HLADR was distributed in the 10^1–10^3 interval, and its expression was relatively low. The proportion of $CD105^-HLA\text{-}DR^+$ cells in the Q1 quadrant was 60.8 %, and the proportion of $HLA\text{-}DR^-CD105^-$double-negative cells in the Q4 quadrant was 39.1 %. In a word, CD73 and CD105 were specifically highly expressed in ADSCs, while the expressions of CD34 and HLA—DR were relatively low, indicating that ADSCs could meet the mesenchymal stem cell phenotypic criteria defined by the International Society for Cell Therapy (ISCT).

3.4. ADSC transplantation combined with the CR promotes wound healing in T2DM mice

Fig. 4A was the experimental protocol of this study. The body weight of the mice was shown in Fig. 4B. Compared with the control group, the body weight of mice in the T2DM group was slightly decreased. Compared with the T2DM group, there was no significant change in body weight in the ADSCs group, the CR group and the ADSCs+CR group. As shown in Fig. 4C, compared with the control group, the FBG levels in the T2DM group, the ADSCs group, the CR group, and the ADSCs group +CR group were all higher than 11.1 mmol/L, and remained at a high level throughout the experiment. As shown in Fig. 4D, on the 5th day after surgery, there was no significant difference in wound healing among the groups. However, 13 days after the operation, the wound area of each group was obviously decreased. Compared with the T2DM group, the healing effects of the control group, the ADSCs group and the CR group were better, while the healing effect of the ADSCs+CR group was the best. The result of the wound closure rate shown in Fig. 4E also indicated this. This indicated that the CR combined with the ADSCs treatment could effectively promote wound healing.

As shown in Fig. 5A-D, compared with the control group, the contents of TNF-α, IFN-γ, IL-1β and MDA in the T2DM group were significantly increased ($p < 0.01$). Compared with the T2DM group, the contents of TNF-α, IFN-γ, IL-1β and MDA in the ADSCs group, the CR group and the ADSCs+CR group were all evidently decreased ($p < 0.01$). Compared with the ADSCs group, the contents of TNF-α, IFN-γ, IL-1β and MDA in the ADSCs+CR group were obviously decreased ($p < 0.01$). Compared with the CR group, the contents of TNF-α, IFN-γ, IL-1β and

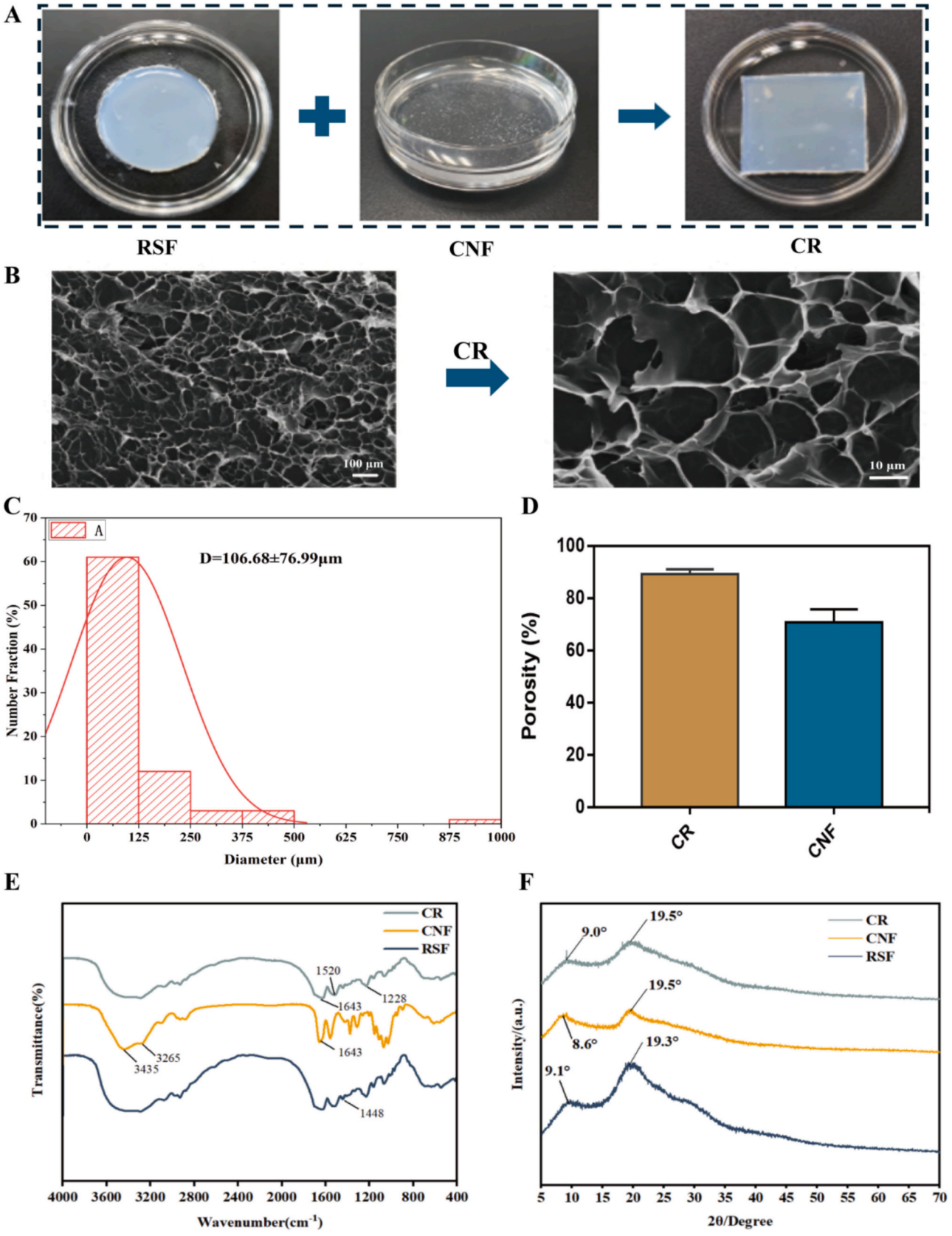

Fig. 1. Characterization of the RSF, the CNF and the CR. (A) Appearance images prepared by the CR. (B) SEM image of the CR (scale: 100 μm on the left, 20 μm on the right). (C) pore size analysis of CR. (D) Porosity of CR and CNF. (E) FTIR spectra of the RSF, the CNF and the CR. (F) XRD spectra of the RSF, the CNF and the CR.

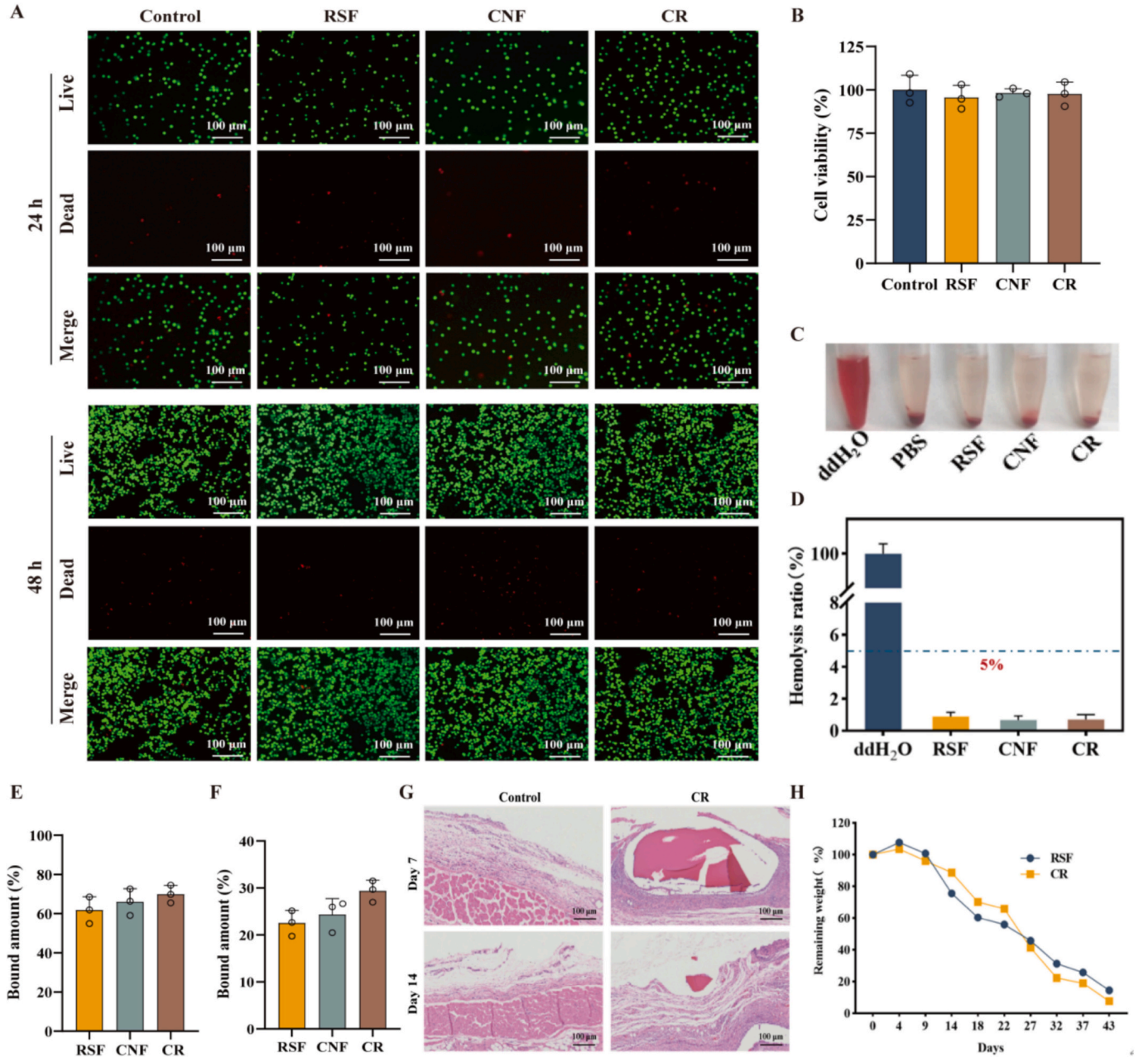

Fig. 2. In vitro biocompatibility experiment of the RSF, the CNF and the CR. (A) Staining diagram of living/dead cells (scale: 100 μm). (B) CCK-8 cytotoxicity test of the RSF, the CNF and the CR. (C) Visual images of the hemolysis test and (D) hemolysis rate. (E) In vitro binding rate of the RSF, the CNF and the CR to TNF-α. (F) In vitro binding rate of the RSF, the CNF and the CR to IFN-γ. (G) H&E staining image of the CR degradation in vivo (scale: 100 μm). (H) In vitro degradation rates of the RSF and the CR.

MDA in the ADSCs+CR group significantly decreased ($p < 0.01$). As shown in Fig. 5E-F, compared with the control group, the contents of SOD and CAT in the T2DM group were obviously decreased ($p < 0.01$). Compared with the T2DM group, the contents of SOD and CAT in the ADSCs group, the CR group and the ADSCs+CR group were significantly increased ($p < 0.01$). Compared with the ADSCs group, the content of CAT in the ADSCs+CR group was evidently increased ($p < 0.01$). Compared with the CR group, the contents of SOD and CAT in the ADSCs+CR group were sensibly increased ($p < 0.05$).

3.5. The CR combined with the ADSCs promotes the regeneration and repair of wound tissues in T2DM mice

The results were shown in Fig. 6A. Compared with the control group, the T2DM group showed certain signs of injury, and the newly formed tissue was very small. Compared with the T2DM group, after treatment with the ADSCs and the CR, the tissue structure gradually became clear, but tissue damage was still shown in some areas. However, compared to the T2DM group, at the edge of the regenerated tissue in the ADSCs+CR group, the formation of skin accessory structures such as hair follicles (red arrow) and sebaceous glands (black arrow) could be observed, and thicker granulation tissue was also observed. Subsequently, masson staining was used to observe the content and arrangement of collagen fibers at the wound site. As shown in Fig. 6B, compared with the control group, the collagen fibers in the T2DM group were sparse and irregular, and collagen synthesis was impaired. Compared with the T2DM group, the content of collagen fibers in the ADSCs group and the CR group was increased, but the arrangement was still uneven. Compared with the

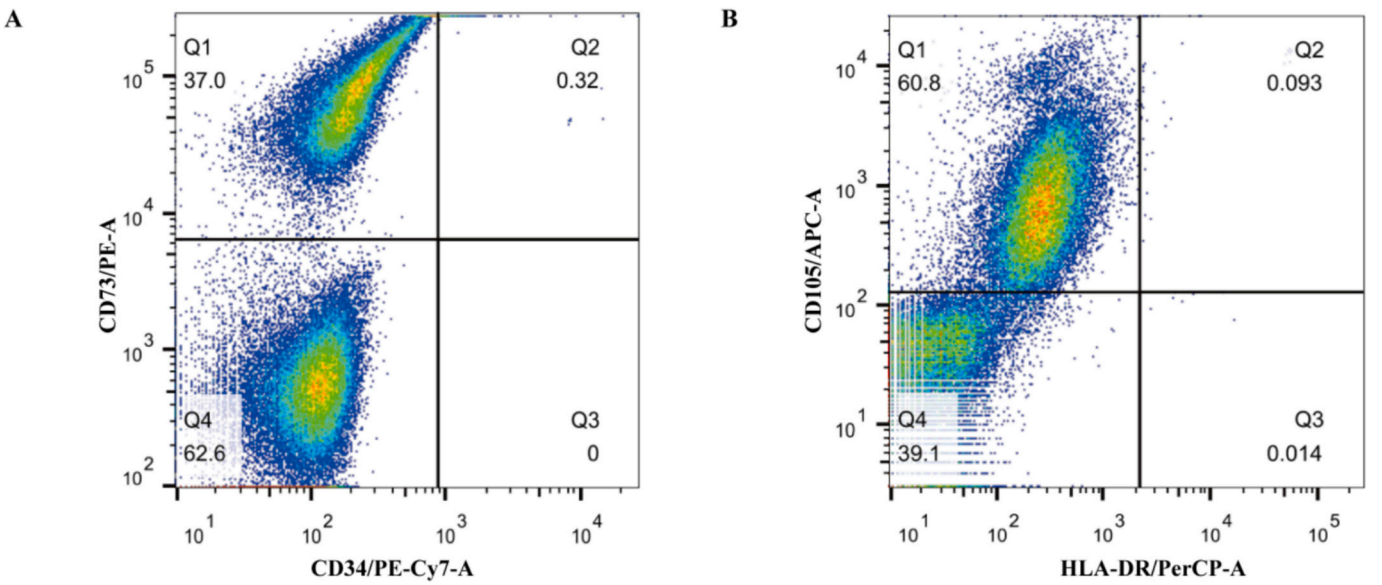

Fig. 3. Flow cytometry detection of surface antigen markers of the ADSCs. CD73 and CD105 represent the positive expression of surface marker proteins of the ADSCs. CD34 and HLA-DR represent negative expression of surface marker proteins of the ADSCs.

ADSCs group and the CR group, the collagen fibers in the ADSCs+CR group were abundant and arranged in a more orderly manner.

As shown in Fig. 6C, compared with the control group, the collagen volume fraction in the T2DM group was significantly decreased ($p < 0.05$). Compared with the T2DM group, the collagen volume fractions of the ADSCs group, the CR group and the ADSCs+CR group were all significantly increased ($p < 0.05$). Compared with the ADSCs group and the CR group, the volume fraction of collagen in the ADSCs+CR group was obviously increased ($p < 0.05$). As shown in Fig. 6D-G, the immunohistochemical staining results of Ki67, collagen I and III on the 7th day were presented to evaluate cell proliferation and collagen production in vivo. Compared with the control group, the expression of Ki67 in the T2DM group was evidently decreased ($p < 0.05$). Compared with the T2DM group, the ADSCs+CR group showed the strongest positive expression of Ki67 ($p < 0.01$). In the immunohistochemical staining results of Collagen I and Collagen III, it was found that the expression levels of the two types of collagen in the ADSCs+CR group were significantly higher than those in the T2DM group ($p < 0.01$), followed by the ADSCs and the CR groups ($p < 0.05$).

3.6. The CR combined with the ADSCs regulates angiogenesis in wounds and the expression of macrophages

The results were shown in Fig. 7, the results of α-SMA staining indicated that the fluorescence intensity was lower in the control group and even worse in the T2DM. However, the fluorescence intensity increased after treatment with the ADSCs and the CR, and the highest expression of α-SMA was observed in the ADSCs+CR group. Compared with the control group, the expression of VEGF in the T2DM group was decreased. Compared with the T2DM group, the expression of VEGF was increased in the ADSCs group and the CR group. Compared with the ADSCs group and the CR group, the expression level of VEGF in the ADSCs+CR group was increased. These results indicated that the treatment of the CR combined with the ADSCs had the strongest effect in promoting neovascularization and could effectively accelerate the wound healing speed.

As shown in Fig. 8, compared with the control group, the expression of CD86 in the T2DM group was significantly increased ($p < 0.01$), while the expression level of CD163 was obviously decreased ($p < 0.01$). Compared with the T2DM group, the expression levels of CD86 in the ADSCs group, CR group and ADSCs+CR group were sensibly decreased ($p < 0.05$), while the expression levels of CD163 in the ADSCs group and ADSCs+CR group were significantly increased ($p < 0.05$). Compared with the CR group, the expression of CD86 in the ADSCs+CR group was evidently decreased ($p < 0.05$), and the expression of CD163 was significantly increased ($p < 0.05$). Compared with the ADSCs group, the expression of CD163 in the ADSCs+CR group was obviously increased ($p < 0.05$).

3.7. Results and analysis of proteomics in T2DM mice

As shown in Fig. 9A, the distribution length of the peptide segments is mainly 7 to 20 amino acids, which conforms to the general rule based on the fragmentation mode of enzymatic hydrolysis and mass spectrometry. It can be seen from Fig. 9B that most proteins correspond to more than two peptide segments. It can be known from the results that the mass spectrometry data can meet the quality control requirements. As shown in Fig. 9C, the pearson correlation coefficient was calculated for the intensity values of all samples. The heat map showed that the samples within the group had a strong correlation, while there were differences among the samples between the groups. As shown in Fig. 9D, principal component analysis was conducted on the relevant quantitative values of all samples. The results indicated that the data within the groups were aggregated, while the data between groups were discrete, suggesting good sample repeatability. As shown in Fig. 9E, the heat map analysis of the differentially expressed proteins in the two groups revealed that there were significant differences in their relative expression levels. The differential proteins were screened with changes in differential expression levels >1.5 or < 1.5 ($p < 0.05$), among which 581 proteins were up-regulated and 567 proteins were down-regulated (Fig. 9F).

In order to further describe the enrichment of KEGG pathway of differential proteins, up-regulated proteins and down-regulated proteins were enriched respectively, as shown in Fig. 9G and Fig. 9H. We found that asthma, viral myocarditis and PPAR signaling pathway were up-regulated, while down-regulated pathways included ribosomes, splices and *staphylococcus aureus* infection. Among the pathways obtained from the above enrichment analysis, we found that the PPAR signaling pathway was involved in processes such as inflammation regulation, angiogenesis, cell proliferation and differentiation. To further reveal the role of the PPAR signaling pathway in wound healing, it was visualized, as shown in Fig. 9I.

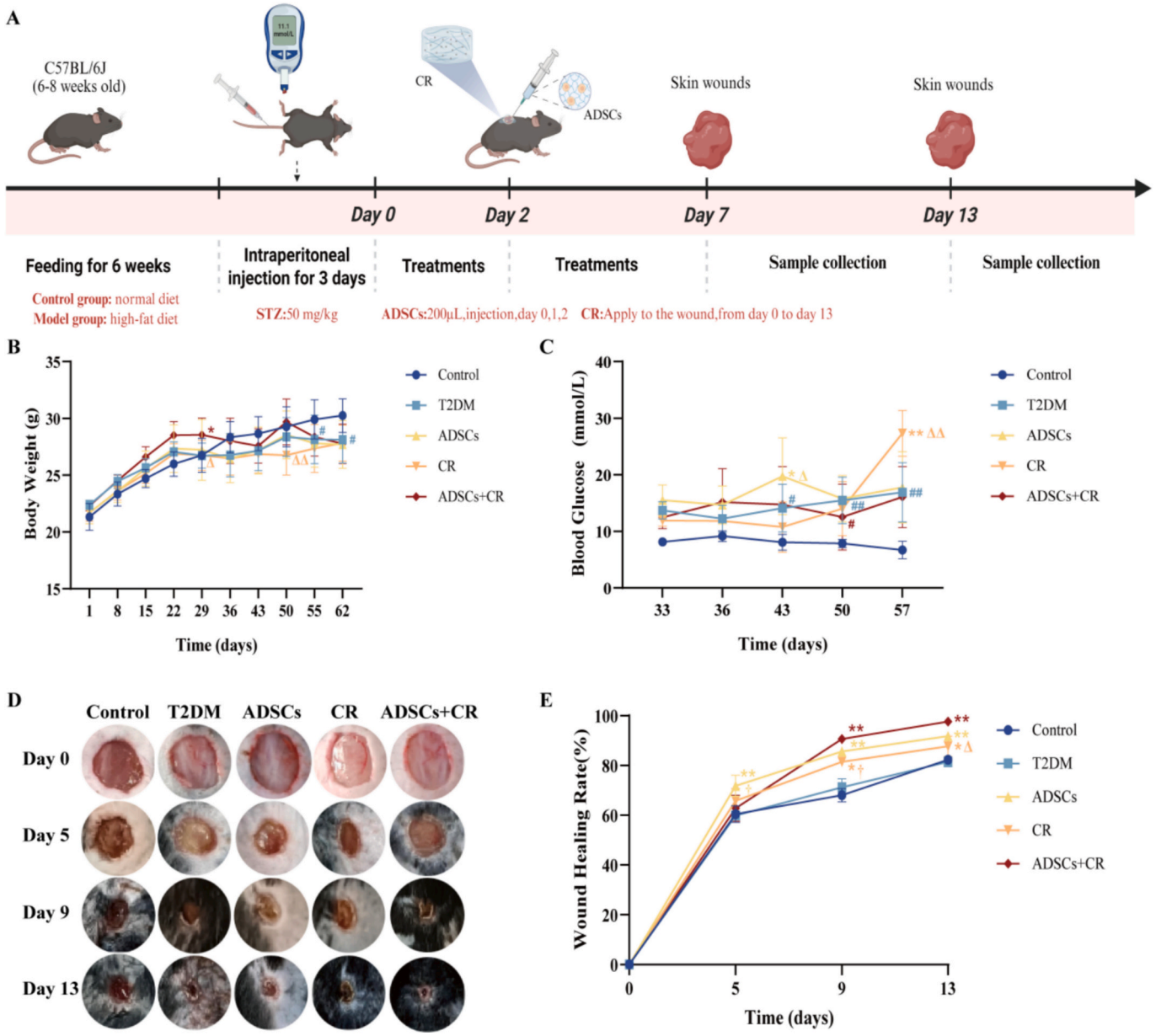

Fig. 4. Wound healing process and histological evaluation in T2DM mice. (A) Diagram of the experimental process. (B) The body weight of mice. (C) The FBG value of mice. (D) Representative images of wound closure in mice. (E) Wound closure rate at different time points after trauma (%). All data were expressed as mean ± SD. $^{\#\#}p < 0.01$, compared with the control group. $^{**}p < 0.01$ and $^{*}p < 0.05$, compared with the T2DM group. $^{\dagger}p < 0.05$, the ADSCs+CR group compared with the ADSCs group. $^{\Delta\Delta}p < 0.01$ and $^{\Delta}p < 0.05$, the ADSCs+CR group compared with the CR group.

3.8. The CR combined with the ADSCs promotes the expression of PPAR-γ, MMP-1, SCD-1 and ACOX2 in the wounds of T2DM mice

As shown in Fig. 10A-E, compared with the control group, the protein expression levels of PPAR-γ and ACOX2 in the T2DM group were evidently decreased ($p < 0.01$), and the protein expression levels of MMP-1 and SCD-1 were sensibly increased ($p < 0.01$). Compared with the T2DM group, the expressions of PPAR-γ and ACOX2 were significantly increased in the CR and the ADSCs+CR groups ($p < 0.05$). Compared with the CR group and the ADSCs group, the expression of PPAR-γand ACOX2 was significantly increased in the ADSCs+CR group ($p < 0.05$). Compared with the T2DM group, the expression of SCD-1 was significantly decreased in the ADSCs, the CR and the ADSCs+CR groups ($p < 0.05$). Compared with the T2DM group, the expression of MMP-1 was significantly decreased in the CR and the ADSCs+CR groups ($p < 0.05$). Compared with the CR group and the ADSCs group, the expression of MMP-1 was significantly decreased in the ADSCs+CR group ($p < 0.05$). Compared with the ADSCs group, the expression of SCD-1 was significantly decreased in the ADSCs+CR group ($p < 0.01$).

4. Discussion

Normally, when the human skin is damaged, the body will initiate a series of complex and orderly repair processes, including hemostasis, inflammation, proliferation, so as to achieve the purpose of wound healing [29]. However, due to its unique pathophysiological characteristics, such as decreased angiogenesis, changes in the composition of extracellular matrix (ECM), and destruction of tissue structure, the healing process of diabetic chronic wounds is often significantly delayed or even difficult to heal [30–32]. These pathological changes together constitute a complex background that chronic wounds of diabetes are difficult to heal, which poses a more severe challenge to traditional

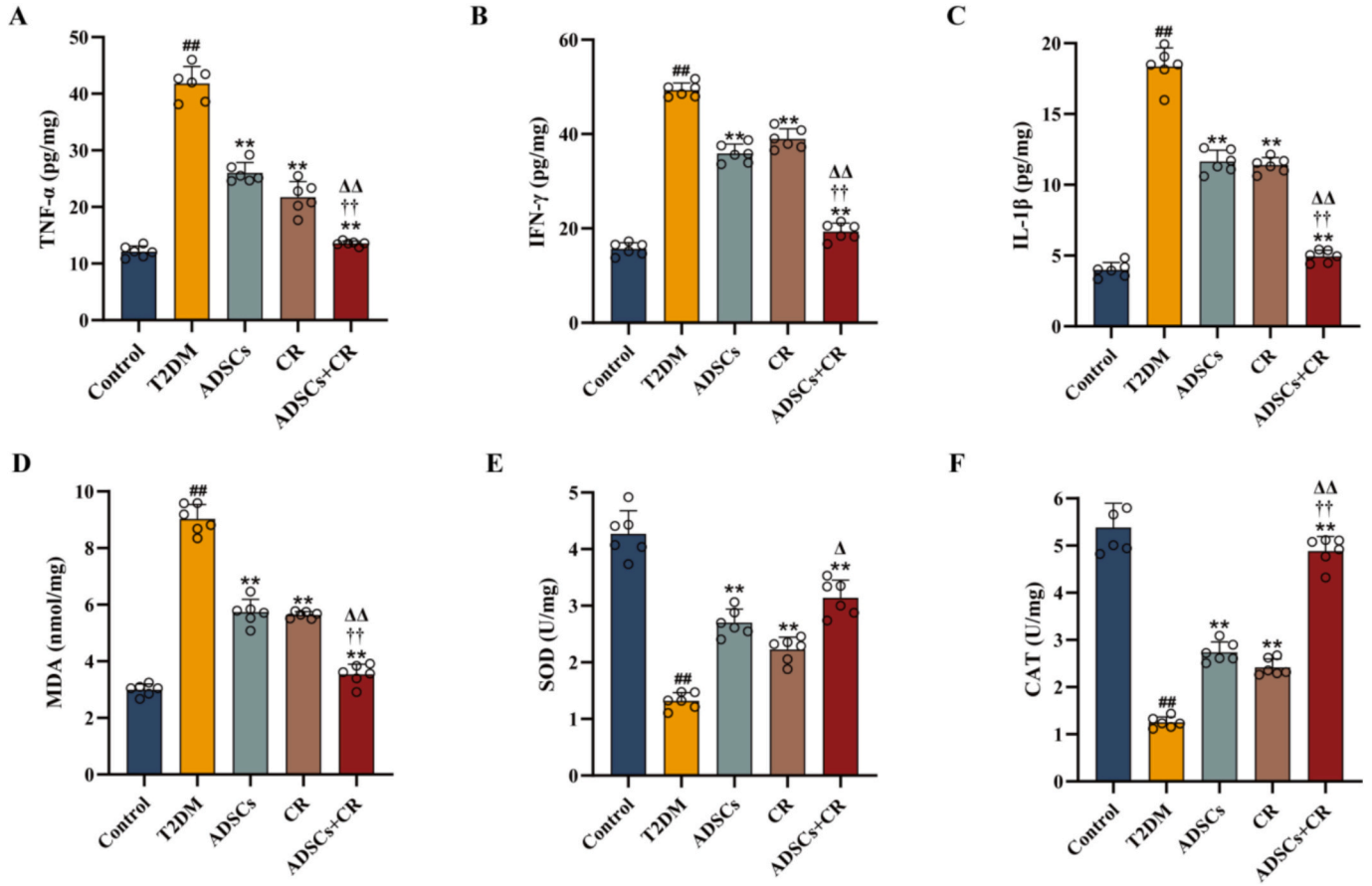

Fig. 5. The changes of inflammatory factors and oxidative stress in wound tissues of T2DM mice. (A–C) The changes in the levels of TNF-α, IFN-γ and IL-1β in wound tissues of T2DM mice. (D—F) The changes of SOD, MDA and CAT levels in wound tissues of T2DM mice. All data were expressed as mean ± SD. $^{\#\#}p < 0.01$, compared with the control group. $^{**}p < 0.01$, compared with the T2DM group. $^{\dagger\dagger}p < 0.01$, the ADSCs+CR group compared with the ADSCs group. $^{\Delta}p < 0.05$ and $^{\Delta\Delta}p < 0.01$, the ADSCs+CR group compared with the CR group.

treatment methods. The ADSCs have been increasingly widely applied in the current field of wound repair. The combination of biological dressings for various wound repairs can better avoid microbial infections in the external environment and maintain a moist environment on the wound surface. Therefore, the CR was prepared and combined with the ADSCs transplantation for the repair of chronic wounds in T2DM in this study. The feasibility of the combined application of the two in the repair of wounds in T2DM was studied and explored.

Multiple studies have shown that mesenchymal stem cells can be involved in multiple links of wound repair [33,34]. Among various types of stem cells, ADSCs have a simple extraction method, convenient material acquisition, abundant cell quantity, strong proliferation ability, low immunogenicity, and strong secretory function. They are the first choice for various basic research and clinical applications. In this study, the results of flow cytometry identification showed that our ADSCs positively expressed CD73 and CD105, and negatively expressed CD34 and HLA-DR. The results were consistent with the characteristics of stem cells. However, the application of ADSCs alone in the treatment of chronic diabetic wounds still has significant limitations. The primary limiting factor lies in the survival rate and functional stability of ADSCs in the microenvironment of the target tissue after transplantation [35]. The pathological microenvironment specific to diabetic wounds, such as high glucose, hypoxia, excessive inflammation and accumulation of reactive oxygen species, can significantly reduce the survival rate and homing efficiency of ADSCs [36], thereby limiting their long-term efficacy. Studies have shown that the survival time of ADSCs in the local area of diabetic wounds is relatively short, usually only lasting for a few days, which makes it difficult to maintain their pro-angiogenic and immunomodulatory effects [37]. Secondly, the chronic inflammatory microenvironment and oxidative stress of the wound surface may inhibit the paracrine function and immunomodulatory activity of ADSCs [38].

In addition, the lack of effective carriers or scaffolds for support is also a key constraint factor [39]. This not only makes it difficult for ADSCs to remain in the wound for a long time and exert continuous effects, but also the exposed wound lacking physical barriers makes the transplanted cells vulnerable to the threat of bacterial colonization [40], further weakening their effect in promoting angiogenesis and tissue regeneration. It is worth noting that although the early-developed stem cell scaffolds provided cell vectors, they still had limitations. Insufficient mechanical performance can easily lead to premature collapse of the stent in a dynamic wound environment [41]. The natural materials commonly used in the early days, such as collagen, gelatin, and alginate, have good biocompatibility, but their degradation rate is difficult to accurately control and their sources are unstable [42]. The mechanical properties and degradation rate of synthetic polymer materials can be adjusted through chemical structure, but degradation products (such as lactic acid) may accumulate locally, triggering inflammatory responses or acidic microenvironments, and inhibiting cell functions [43]. The microstructure of early scaffolds is difficult to simulate the three-dimensional microenvironment of natural tissues, resulting in limited cell function and a lack of key biological functions such as active regulation of inflammation and elimination of excessive inflammatory factors [44]. In contrast, the CR prepared in this study has excellent biocompatibility and controllable degradability, and its three-dimensional porous structure is conducive to cell infiltration and material exchange. In particular, CR can effectively isolate key pro-

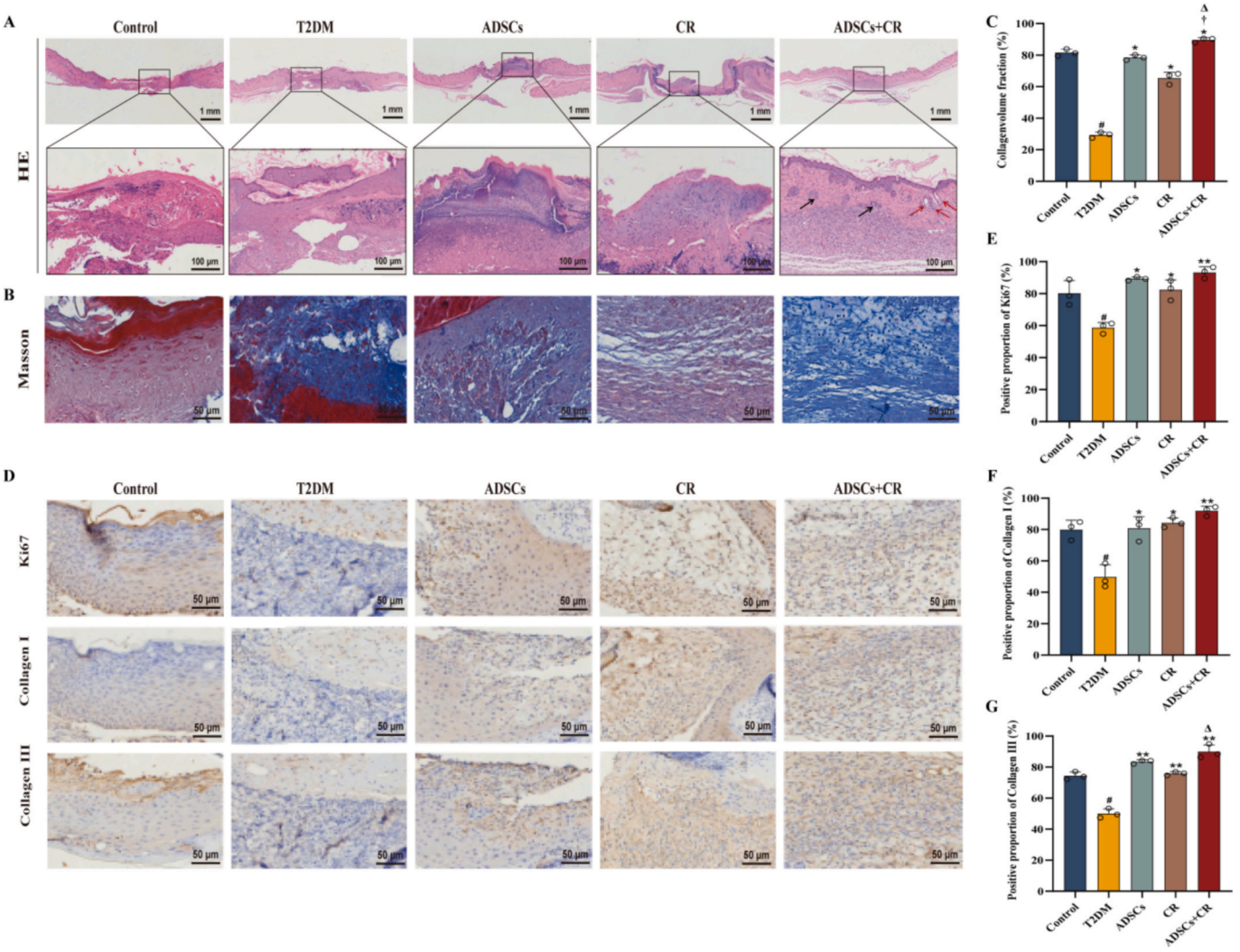

Fig. 6. Histopathological evaluation of wounds in T2DM mice. (A) On the 7th day, the wound surface of the mice was stained with HE, red arrow: hair follicle, black arrow: Sebaceous gland, (Scale: 1 mm, 100 μm). (B—C) Masson staining and statistical analysis of the wound surface of mice on the 7th day. (D-G) Immunohistochemical staining and statistical analysis of Ki67, Collagen I and Collagen III on the 7th day. (Scale: 50 μm). All data were expressed as mean ± SD. $^{\#}p < 0.05$, compared with the control group. $^{**}p < 0.01$ and $^{*}p < 0.05$, compared with the T2DM group. $^{\dagger}p < 0.05$, the ADSCs+CR group compared with the ADSCs group. $^{\Delta}p < 0.05$, the ADSCs+CR group compared with the CR group.

inflammatory factors, thereby improving the local microenvironment of transplantation and providing a better survival and functional platform for ADSCs. Zhang et al. also reported that intelligent responsive hydrogels can neutralize acidic microenvironments and reduce stem cell apoptosis [45]. Therefore, the combined application of CR and ADSCs is an important strategy in the field of wound repair. The limitation of this study is that the survival rate and retention of ADSCs were not tracked. It will continue to be tracked in subsequent experiments.

In this study, the RSF and the CNF were prepared from silk and squid cartilage, and then they were mixed and placed at room temperature for cross-linking to finally prepare the CR. Its physical and chemical properties were characterized to understand the structure of the CR and its degradation ability in vivo and in vitro. The three-dimensional porous structure of the CR could be observed through SEM and the pore distribution was uniform. This structure may enable the CR to both absorb wound secretions and maintain a moist environment, thereby maintaining a relatively favorable local moist environment for healing. In nature, the molecular chains of β-chitin are arranged in parallel, which has better reaction characteristics, swelling property and solvent affinity [46,47]. From the FTIR and XRD results, it can be seen that the composite material with added β-chitin exhibits an amorphous structure and lower crystallinity, which makes the CR have a good three-dimensional porous structure. Both in vivo and in vitro degradation experiments have demonstrated that the CR had good degradation ability. However, the different degradation times may be affected by physiological environment, temperature and PH, and different enzymatic hydrolysations in vivo and in vitro.

Good biocompatibility is the foundation for the application of materials in wound repair, which helps to achieve faster and more effective wound healing and reduce potential complications [48,49]. The biocompatibility results showed that there were a large number of living cells (green) and a very small number of dead cells (green) in each group at 24 h, and the growth and proliferation of cells in each group were good after 48 h. Subsequently, the toxic effect of the material on L929 cells was further detected by CCK-8. According to ISO 10993-5:2009, when the cell viability exceeds 70 %, this material is recognized as having good biocompatibility [50]. Our results displayed that the cell viability of each group was all greater than 90 %, and it was considered that there was no obvious toxic effect. These results indicated that the material had good cell compatibility. In addition, the results of the hemolysis test showed that the hemolysis rate of each group of materials was below the biological safety standard of 5 %, indicating that there

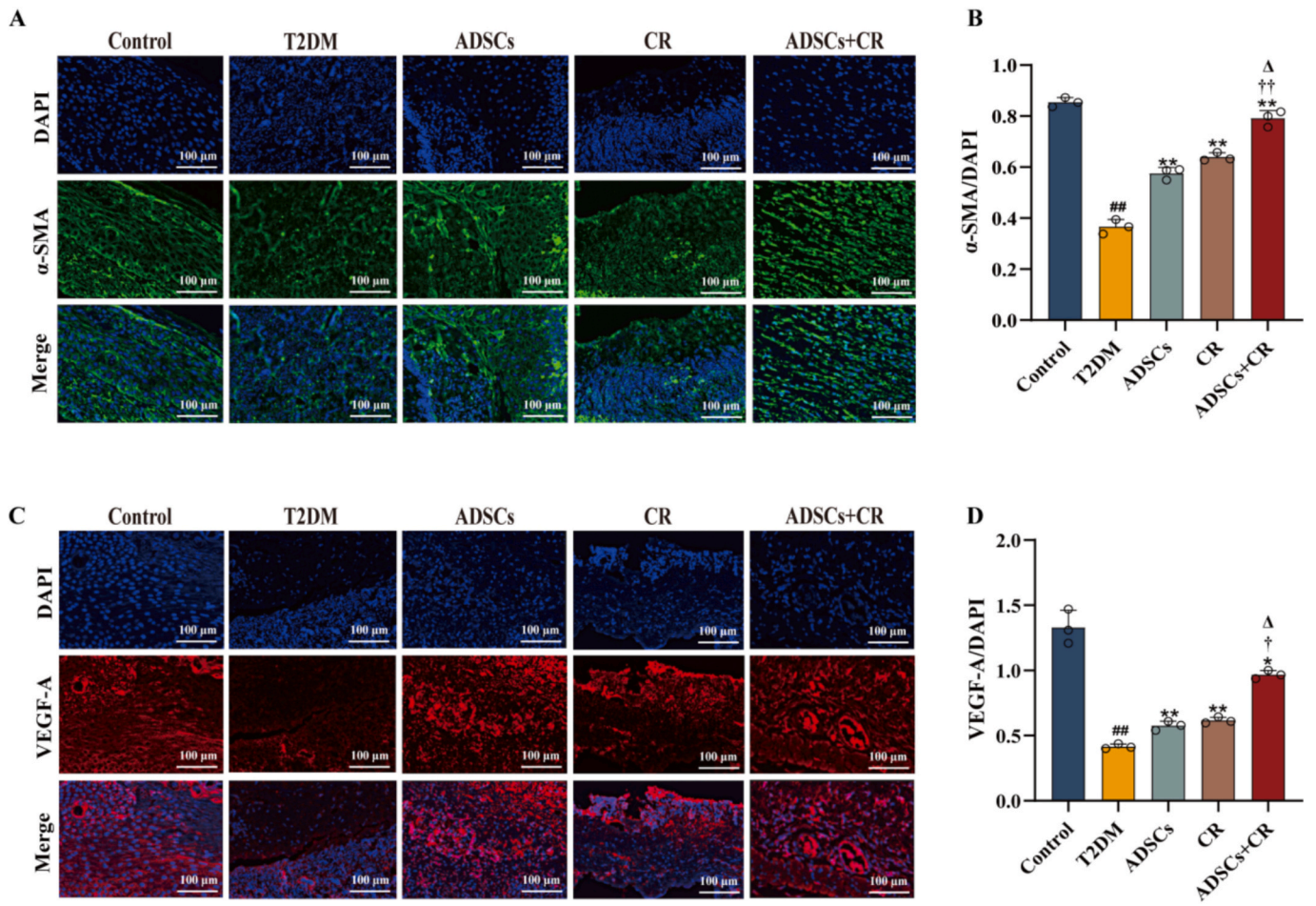

Fig. 7. Immunofluorescence staining images of mouse wounds on the 7th day. (A-B) Representative immunofluorescence images and quantification images of α-SMA in the wound area of mice in each group on the 7th day. (C—D) Representative immunofluorescence images and quantification images of VEGF-A in the wound area of mice in each group on the 7th day. All data were expressed as mean ± SD. $^{\#\#}p < 0.01$, compared with the control group. $^{**}p < 0.01$, compared with the T2DM group. $^{\dagger\dagger}p < 0.01$ and $^{\dagger}p < 0.05$, the ADSCs+CR group compared with the ADSCs group. $^{\Delta}p < 0.05$, the ADSCs+CR group compared with the CR group.

was no significant hemolysis reaction in the materials, thus confirming their good blood compatibility. This excellent biocompatibility is likely attributed to the fact that all the raw materials for preparation are sourced from nature and have no toxic effects on the human body, ensuring the safety and reliability of the material in clinical applications.

Wound repair is a dynamic and interactive process, which can be divided into three overlapping phases: the inflammatory phase, the proliferative phase and the remodeling phase [51]. Inflammation is an immune response process caused by the body's exposure to harmful stimuli from the external environment. Chronic and excessive inflammation can delay the repair of wounds or even prevent them from healing. Therefore, good inflammation regulation can ensure wound repair. During the inflammatory response process, TNF-α is one of the earlier released pro-inflammatory response factors [52]. TNF-α plays an overall regulatory role in the inflammatory process by promoting the aggregation and activation of inflammatory cells and the secretion of inflammatory factors [53]. IFN-γ is an important cytokine, mainly secreted by activated T cells and natural killer (NK) cells, and plays a key role in immune regulation and inflammatory responses [54]. In this study, the biocompatibility and bioactivity of CR can be understood by detecting the binding rate of CR to TNF-α and IFN-γ. Subsequently, the binding experiments of TNF-α and IFN-γ were conducted in vitro, which proved that the RSF, the CNF and the CR all had strong isolation effects on TNF-α and IFN-γ, which was consistent with that reported in many literatures [55–57].

Under the condition of diabetes, oxidative stress caused by high blood sugar will continuously stimulate local tissues to release TNF-α and IFN-γ [58]. This is consistent with the findings of this study. TNF-α and IFN-γ can strongly induce macrophages to polarize towards M1 type [58]. M1-type macrophages not only further secrete a large amount of TNF-α and IFN-γ, but also release pro-inflammatory factors such as IL-1β and IL-6, forming an inflammatory cascade amplification effect of "pro-inflammatory factors inducing M1-type polarization - M1-type macrophages secreting more pro-inflammatory factors" [59]. The results of this study also revealed abnormal changes in TNF-α, IFN-γ, IL-1β and IL-6. This effect can lead to a persistent local inflammatory response at the wound site. Excessive inflammation can disrupt the formation of new blood vessels, inhibit the proliferation of fibroblasts and the synthesis of collagen, and also degrade the extracellular matrix, hindering the normal healing process of the wound [60]. In addition, the persistent dominance of M1-type macrophages will also inhibit the polarization of M2-type macrophages, which play an important role in promoting tissue regeneration and anti-inflammation during the proliferation and remodeling stages of wound repair, and the inhibition of their functions further aggravates the delay of diabetic wound healing [61]. In this study, it was found that the expression of M1 macrophage marker CD86 in the model group was significantly higher than that in the control group. The combined application of CR and ADSCs can not only effectively inhibit the polarization of M1-type macrophages induced by TNF-α and IFN-γ and its inflammatory cascade amplification effect, but also promote the polarization of M2-type macrophages, creating a suitable microenvironment for wound healing, thus accelerating the healing of

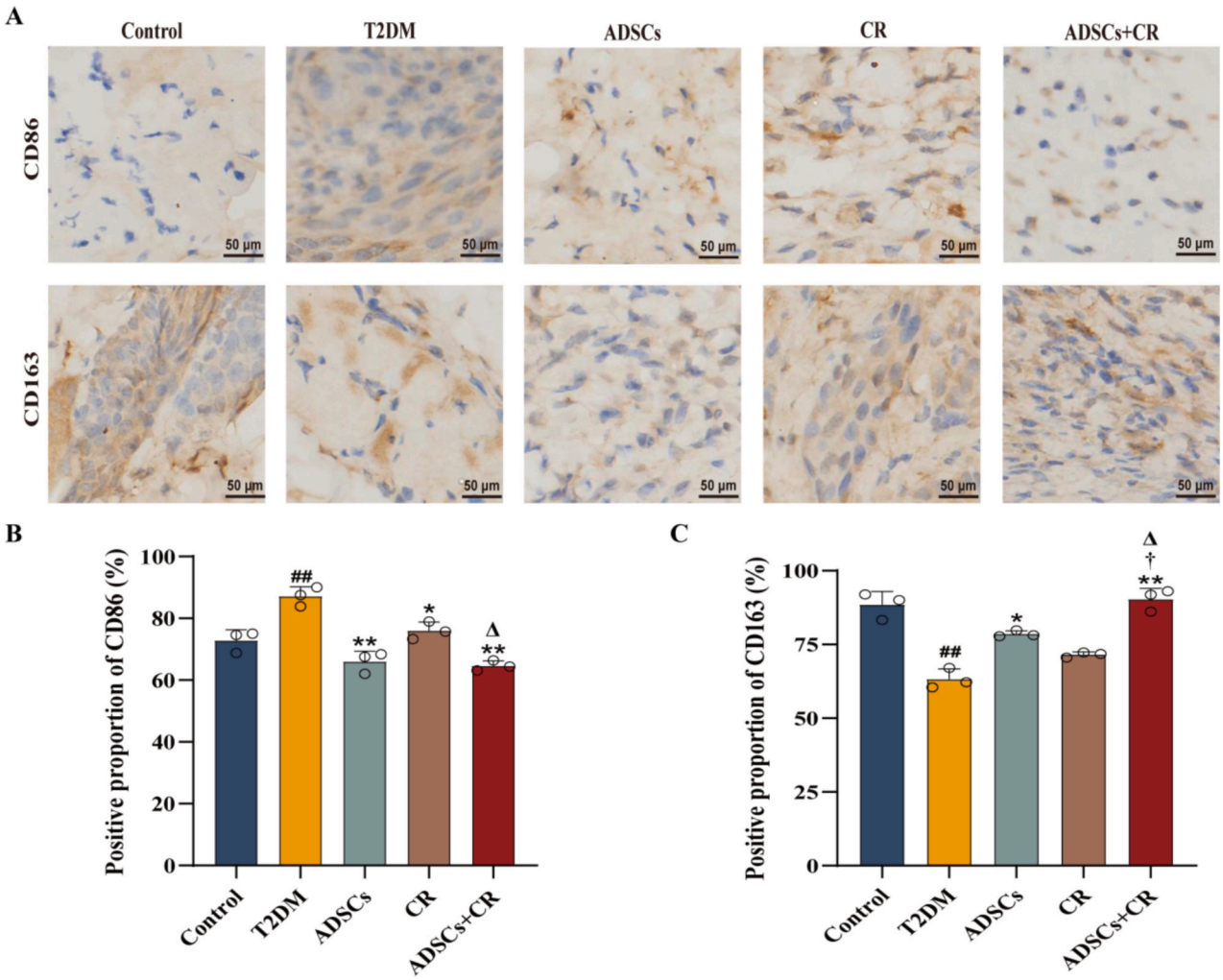

Fig. 8. The effect of CR combined with ADSCs on the expression of macrophages. (A) Immunohistochemical staining of CD86 and CD163 on the 7th day of the wound. (B) Statistical results of CD86 immunohistochemical staining positive cells. (C Statistical results of CD 163 immunohistochemical staining positive cells. All data were expressed as mean ± SD. $^{\#\#}p < 0.01$, compared with the control group. $^{**}p < 0.01$ and $^{*}p < 0.05$, compared with the T2DM group. $^{\dagger}p < 0.05$, the ADSCs+CR group compared with the ADSCs group. $^{\Delta}p < 0.05$, the ADSCs+CR group compared with the CR group.

diabetic wounds. The combined application of CR and ADSCs still has a mechanism of synergistic enhancement. ADSCs injected alone are prone to apoptosis due to inflammatory factor stimulation and oxidative stress factors in the complex microenvironment of the wound surface, and will also significantly weaken the immunomodulatory function of ADSCs [36]. The dense pore distribution of CR can effectively block the penetration of bacteria and reduce the chance of bacterial colonization in wound tissue [62]. The CR may improve the local microenvironment, improve the survival rate of ADSCs and promote their retention, which may be one of the reasons why CR + ADSCs group has a better effect.

The experimental results showed that during the entire modeling period, compared with the control group, there was no significant change in the body weight of mice in the other groups. From the perspective of FBG levels, the FBG of mice in the control group was always lower than 11.1 mmol/L, while the FBG levels of mice in other groups were significantly increased and remained at a high level throughout the experiment. The results showed that STZ combined with HFD successfully induced an increase in FBG in mice of the T2DM group, meeting the diagnostic criteria for diabetes. The reason for this result might be due to the damage or destruction of pancreatic β cells, resulting in insufficient insulin secretion and inability to effectively reduce FBG levels [63,64]. From the results of wound healing, the wound healing rate of mice in each group was similar on the fifth day, and there was no significant difference. On the 13th day, compared with the T2DM group, the ADSCs + CR group could effectively promote wound healing in T2DM mice. The wound closure rate of the ADSCs + CR group was higher than that of the CR group and the ADSCs group, and it almost completely healed on the 13th day. It was speculated that this result might be due to the simultaneous exertion of the synergistic effect between the CR and the ADSCs, generating an effect of "1+1 > 2".

Cell proliferation and wound reepithelialization are two stages in the wound healing process, which are of great significance for restoring the integrity and function of damaged tissues [65]. After activation, epithelial cells began to proliferate and move towards the wound surface, forming a new epithelial layer [66]. The proliferating fibroblasts secrete ECM near the wound surface, which provides support for the migration of epithelial cells and promotes the re-epithelization [67]. An in vitro study demonstrated that Rab37 promotes the proliferation, migration and endothelial differentiation of the ADSCs and accelerates the healing of diabetic wounds mediated by the ADSCs [68]. The ADSCs can also help repair the tissue structure of wounds by synthesizing and secreting ECM components. The results of HE staining showed that compared with the T2DM group, the ADSCs+CR group generated a large amount of granulation tissue and some skin appendage, and had the highest epithelial coverage rate. The masson staining results indicated that compared with the CR group and the ADSCs group, the collagen

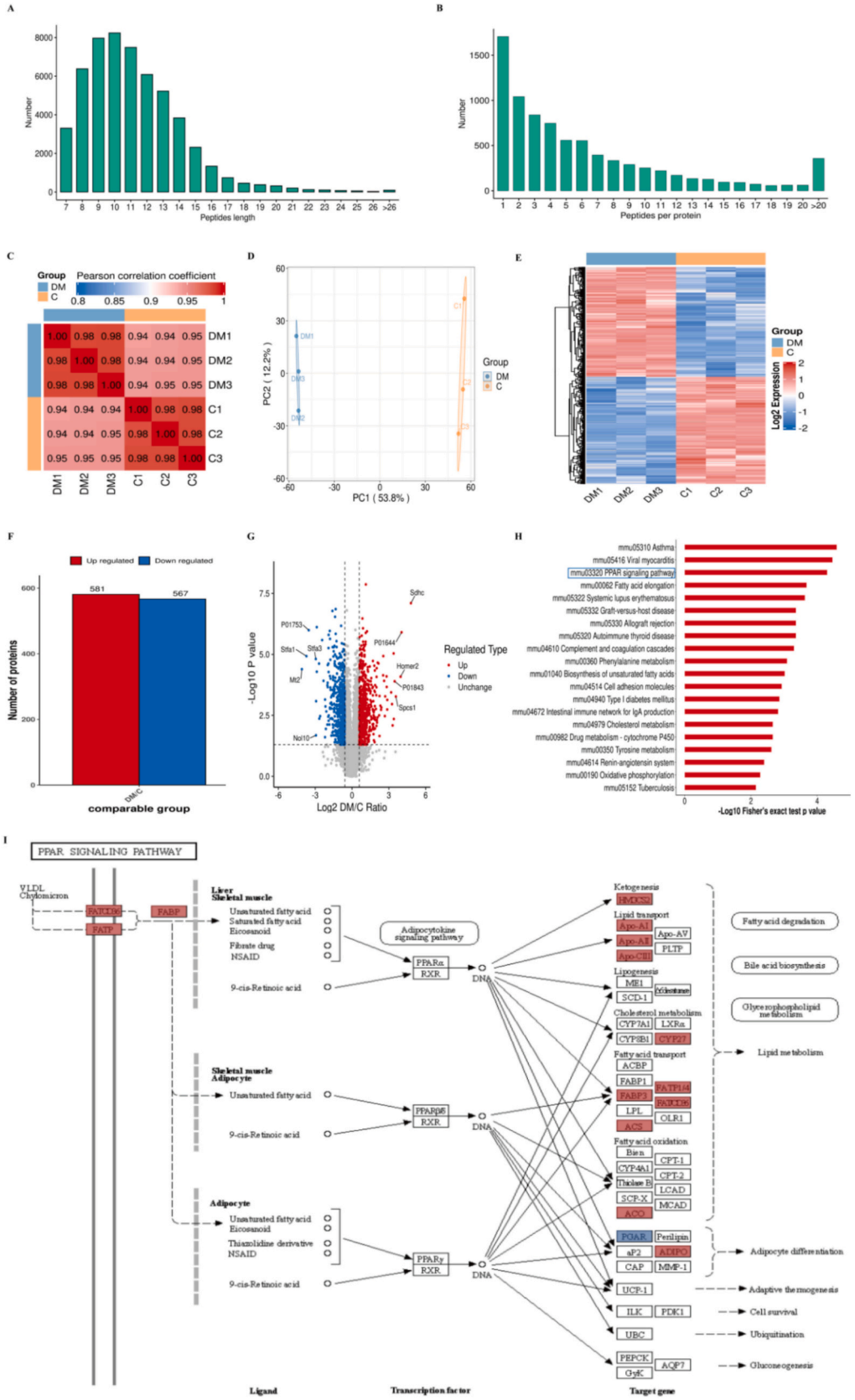

Fig. 9. Proteomic analysis of the control group and the T2DM group. (A) Protein peptide length profile. (B) Number distribution of protein peptides. (C) Pearson Correlation Coefficient (PCC) heat map. (D) Principal Component Analysis (PCA) graph. (E) Clustering heat maps of differential proteins in the control group and the T2DM group, with red representing up-regulated genes and blue representing down-regulated genes. (F) Quantitative analysis diagram of differential proteins. (G) Volcano plots of differentially expressed proteins, with red representing significantly differentially upregulated proteins and blue representing significantly differentially downregulated proteins. (H) Enrichment analysis of the upregulated protein KEGG pathway. (I) Visualization of the PPAR signaling pathway.

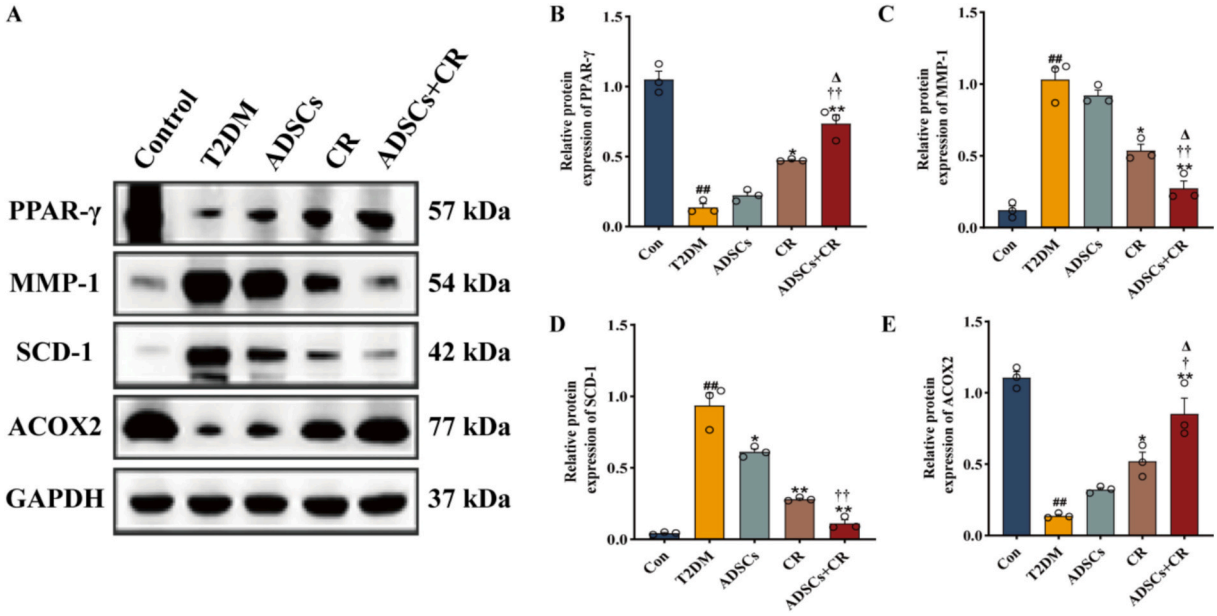

Fig. 10. Effect of ADSCs+CR on PPAR-γ signaling pathway protein expression. (A-E) Protein expression and quantitative analysis of PPAR-γ, MMP-1, SCD-1 and ACOX2 in mice wound on the 13th day. All data were expressed as mean ± SD ($n = 3$). $^{\#\#}p < 0.01$, compared with the control group. $^{**}p < 0.01$ and $^{*}p < 0.05$, compared with the T2DM group. $^{\dagger\dagger}p < 0.01$ and $^{\dagger}p < 0.05$, the ADSCs+CR group compared with the ADSCs group. $^{\Delta}p < 0.05$, the ADSCs+CR group compared with the CR group.

fibers generated in the ADSCs+CR group had the richest content and were arranged in a more orderly manner. In this study, masson staining of wound tissue was not observed dynamically at multiple time points in order not to violate the "3R principle" of animal ethics. Furthermore, we also performed immunohistochemical staining on Ki67, Collagen I and Collagen III. The high positive rate of Ki67 indicates that the wound surface is in the active repair stage [69]. Compared with the CR group and the ADSCs group, the ADSCs+CR group had the most positive stained cells and the highest degree of cell proliferation activity. Collagen I and Collagen III are mainly distributed in the dermis and jointly constitute the collagen fiber network of the dermis. Compared with the CR group and the ADSCs group, the expression levels of Collagen I and Collagen III were the highest in the ADSCs+CR group. The ADSCs+CR may have a better ability to promote tissue regeneration and remodeling in wound repair, showing similar results with HE and masson. These results can explain that the CR combined with the ADSCs better promotes cell proliferation, re-epithelialization, and the generation and reconstruction of collagen fibers to accelerate the healing of T2DM wounds. Meanwhile, it also indirectly proves that there was no contamination of ADSCs in the experiment.

The formation of new blood vessels during wound repair is crucial for wound healing, providing oxygen and nutrients to the wound and enhancing the tissue's ability to resist infection [70]. One of the key factors for the difficulty in wound healing in diabetic patients is the reduction of angiogenesis. Due to long-term exposure to a hyperglycemic state, endothelial cells experience dysfunction and loss of integrity, which is the fundamental cause of local microvascular and macrovascular complications. Eventually, it leads to a significant delay in wound closure by affecting angiogenesis [71]. Therefore, promoting vascular regeneration in the process of healing has become one of the key points. In this study, α-SMA and VEGF-A were stained by immunofluorescence to evaluate the angiogenesis during wound healing. The α-SMA is used to identify smooth muscle cells and myofibroblasts, and VEGF-A plays an important role in wound healing and angiogenesis. VEGF-A is the main subtype of VEGF and binds to the receptors on endothelial cells to promote vascular growth. The results demonstrated that compared with the CR group and the ADSCs group, the fluorescence intensities of vascular markers α-SMA and VEGF-A in the ADSCs+CR group were the highest. These results proved that the CR combined with the ADSCs could promote the regeneration of local blood vessels and provide more oxygen and nutrients for the rapid healing of wounds. According to previous reports, this effect of promoting angiogenesis is closely related to the secretion of various growth factors by the ADSCs [72]. The ADSCs have a good effect on enhancing angiogenesis, which can promote the formation of new blood vessels and improve local blood supply to wounds by stimulating the release of angiogenic factors, endothelial growth factor, and basic fibroblast growth factor [73].

However, the mechanism of the CR combined with the ADSCs on the healing of diabetic wounds remains to be studied. Therefore, proteomics sequencing was conducted, and it was found that among the differential proteins, 581 proteins were up-regulated and 567 proteins were down-regulated. Through the enrichment analysis of differential proteins, it was found that the PPAR signaling pathway plays an important role in multiple stages of wound healing. The decreased expression level of PPAR signaling pathway is related to the aggravation of inflammatory reaction, decreased angiogenesis and abnormal cell metabolism, which together lead to delayed wound healing in diabetes mellitus. This study found that the CR combined with the ADSCs can down-regulate the expression of MMP-1 by activating the PPAR-γ signaling pathway. MMP-1 is one of the main enzymes for degrading collagen and is crucial for the remodeling of ECM. Its excessive activation can lead to the destruction of ECM and delay the healing of diabetic wounds [74]. The combined treatment of the CR and the ADSCs can up-regulate PPAR-γ and significantly reduce the expression of MMP-1, thereby protecting ECM from excessive degradation. SCD-1 is a key enzyme in fatty acid metabolism, catalyzing the conversion of saturated fatty acids into monounsaturated fatty acids, and is crucial for maintaining the fluidity and function of cell membranes [75,76]. Under the condition of diabetes, the increased expression of SCD-1 can lead to lipid metabolism disorders, thereby affecting wound healing [77]. The CR combined with the ADSCs treatment can significantly reduce the expression level of SCD-1. ACOX2 is a key enzyme involved in fatty acid oxidation and is involved in the metabolism of branched-chain fatty acids and bile acid intermediates [78]. In diabetic wounds, the expression of ACOX2 is decreased, which may be related to the reduction of fatty acid oxidation and energy metabolism disorders [79]. The combined treatment of the CR and the

ADSCs significantly increased the expression level of ACOX2. This might promote the oxidation of fatty acids by increasing the expression of ACOX2, improve energy metabolism, and be beneficial to cell function and regeneration during the wound healing process. Chang et al. found that the activation of PPAR-γ could lead to expression changes of downstream targets similar to those in this study and exert anti-inflammatory effects [80]. Furthermore, the research also confirmed that the functional abnormality of PPAR-γ would significantly affect the changes of SCD-1 and ACOX2 [81,82], which is consistent with the results of this study. These existing research results provide strong external support for the causal relationship between the PPAR-γ pathway and the core phenomenon in this study. In general, the expression of PPAR-γ in T2DM wounds was up-regulated after the ADSCs+CR intervention, thus regulating the expression of downstream molecules MMP-1, SCD-1 and ACOX2 to accelerate the healing process of diabetes wounds.

It is worth noting that there are gender differences in the wound healing process. Studies have shown that women usually heal faster than men, which may be related to hormone levels, immune response and metabolic characteristics [83]. In particular, estrogen has been proven to regulate multiple healing pathways, including inflammatory responses, angiogenesis, and extracellular matrix remodeling [84]. As a key regulatory factor revealed in this study, the expression and activity of PPARγ are also significantly affected by estrogen [85]. Studies have shown that estrogen can positively regulate the expression and transcriptional activity of PPARγ through the estrogen receptor signaling pathway [86]. Therefore, endogenous estrogen may promote more effective inflammation resolution and tissue regeneration by synergistically enhancing the activity of the PPARγ pathway in female individuals. Nevertheless, male mice still have significant advantages in the study of basic mechanism. On the one hand, its physiological state is relatively stable and less affected by the fluctuations of the hormone cycle, which can reduce the variables and contingency in the experimental process and ensure the reliability and repeatability of the experimental results. On the other hand, male individuals lack the "physiological promotion" effect of estrogen on the healing process, and the wound healing disorder in the state of diabetes can directly reveal the inhibitory effect of pathological microenvironments such as high glucose environment, chronic inflammation and oxidative stress on tissue repair. Under this background, we observed that the combined application of CR and ADSCs showed a remarkable healing effect by activating PPARγ pathway, which strongly proved that the therapeutic strategy could play an active repair role independently of endogenous estrogen. It also avoids the potential interference of endogenous estrogen on the therapeutic effect.

5. Conclusion

In this study, the CR composite material was prepared. In vitro experiments indicated that the CR had a good three-dimensional porous structure, biocompatibility, and degradation performance in vivo and in vitro. In vivo experiment, the T2DM wound model was established through the induction of STZ combined with HFD. We found that the CR combined with the ADSCs transplantation therapy can promote the wound healing of T2DM mice, including promoting wound re-epithelization, collagen deposition, cell proliferation and angiogenesis, and regulating macrophage expression. Proteomic results indicated that CR combined with ADSCs transplantation may improve fat metabolism, alleviate inflammation and oxidative stress, and accelerate wound healing by activating the PPAR - γ signaling pathway. In conclusion, this study provides a solid experimental basis for the wide application of the CR combined with the ADSCs transplantation therapy in various wounds.

CRediT authorship contribution statement

Ziyang Zhang: Writing – original draft, Visualization, Supervision, Methodology. **Yaoyi Zheng:** Software, Methodology, Data curation. **Ziyi Wang:** Methodology, Formal analysis, Data curation. **Yi Li:** Project administration, Formal analysis. **Yunen Liu:** Writing – review & editing, Supervision, Resources, Funding acquisition. **Zhonghua Luo:** Writing – review & editing, Writing – original draft, Funding acquisition.

Fund

The research was supported by the Shenyang Natural Science Foundation Special Project (23–503–6-14) and the Joint Program of Science and Technology Plans of Liaoning Province (2024011888-JH3/4700).

Declaration of competing interest

The authors declare that they have no known competing financial interests or personal relationships that could have appeared to influence the work reported in this paper.

Data availability

The authors do not have permission to share data.

References

[1] W. Chang, Y. Chen, H. Tseng, et al., Gut microbiota in patients with prediabetes, Nutrients 16 (8) (2024) 1105.
[2] Y. Fu, Y. Shi, L. Wang, et al., All-natural immunomodulatory bioadhesive hydrogel promotes angiogenesis and diabetic wound healing by regulating macrophage heterogeneity, Adv Sci (Weinh). 10 (13) (2023) e2206771.
[3] Y. Song, Y. You, X. Xu, et al., Adipose-derived mesenchymal stem cell-derived exosomes biopotentiated extracellular matrix hydrogels accelerate diabetic wound healing and skin regeneration, Adv. Sci. (Weinh.). 10 (30) (2023) e2304023.
[4] S. Li, J. Deng, D. Sun, et al., FBXW7 alleviates hyperglycemia-induced endothelial oxidative stress injury via ROS and PARP inhibition, Redox Biol. 58 (2022) 102530.
[5] J. Yang, Z. Chen, D. Pan, et al., Umbilical cord-derived mesenchymal stem cell-derived exosomes combined Pluronic F127 hydrogel promote chronic diabetic wound healing and complete skin regeneration, Int. J. Nanomedicine 15 (2020) 5911–5926.
[6] F.M. Davis, A. Kimball, A. Boniakowski, K. Gallagher, Dysfunctional wound healing in diabetic foot ulcers: new crossroads, Curr. Diab. Rep. 18 (1) (2018) 2.
[7] N. Yuan, K. Shao, S. Huang, C. Chen, Chitosan, alginate, hyaluronic acid and other novel multifunctional hydrogel dressings for wound healing: a review, Int. J. Biol. Macromol. 240 (2023) 124321.
[8] R.M. Samsonraj, M. Raghunath, V. Nurcombe, et al., Concise review: multifaceted characterization of human mesenchymal stem cells for use in regenerative medicine, Stem Cells Transl. Med. 6 (12) (2017) 2173–2185.
[9] Y. Shingyochi, H. Orbay, H. Mizuno, Adipose-derived stem cells for wound repair and regeneration, Expert. Opin. Biol. Ther. 15 (9) (2015) 1285–1292.
[10] N. Naderi, E.J. Combellack, M. Griffin, et al., The regenerative role of adipose-derived stem cells (ADSC) in plastic and reconstructive surgery, Int. Wound J. 14 (1) (2017) 112–124.
[11] M. Keese, J. Zheng, K. Yan, et al., Adipose-derived mesenchymal stem cells protect endothelial cells from hypoxic injury by suppressing terminal UPR in vivo and in vitro, Int. J. Mol. Sci. 24 (24) (2023) 17197.
[12] P. Kumar, S. Kandoi, R. Misra, et al., The mesenchymal stem cell secretome: a new paradigm towards cell-free therapeutic mode in regenerative medicine, Cytokine Growth Factor Rev. 46 (2019) 1–9.
[13] M. Gadelkarim, A.I. Abushouk, E. Ghanem, et al., Adipose-derived stem cells: effectiveness and advances in delivery in diabetic wound healing, Biomed. Pharmacother. 107 (2018) 625–633.
[14] Y. Chen, X. Wang, S. Tao, et al., Research advances in smart responsive-hydrogel dressings with potential clinical diabetic wound healing properties, Mil. Med. Res. 10 (1) (2023) 37.
[15] S.M. Ahsan, M. Thomas, K.K. Reddy, et al., Chitosan as biomaterial in drug delivery and tissue engineering, Int. J. Biol. Macromol. 110 (2018) 97–109.
[16] S. Patel, A. Goyal, Chitin and chitinase: role in pathogenicity, allergenicity and health, Int. J. Biol. Macromol. 97 (2017) 331–338.
[17] S.E. Svensson, A.O. Oliveira, K.H. Adolfsson, et al., Turning food waste to antibacterial and biocompatible fungal chitin/chitosan monofilaments, Int. J. Biol. Macromol. 209 (Pt A) (2022) 618–630.
[18] A.C. Wan, B.C. Tai, CHITIN–a promising biomaterial for tissue engineering and stem cell technologies, Biotechnol. Adv. 31 (8) (2013) 1776–1785.
[19] S. Khattak, F. Wahid, L.P. Liu, et al., Applications of cellulose and chitin/chitosan derivatives and composites as antibacterial materials: current state and perspectives, Appl. Microbiol. Biotechnol. 103 (5) (2019) 1989–2006.

[20] P. Baharlouei, A. Rahman, Chitin and chitosan: prospective biomedical applications in drug delivery, Cancer treatment, and wound healing, Mar. Drugs 20 (7) (2022) 460.
[21] S. Zhang, H. Chen, H. Ma, et al., A MoS(2)QDs/chitin nanofiber composite for improved antibacterial and food packaging, Int. J. Biol. Macromol. 209 (Pt A) (2022) 737–746.
[22] P. Chen, L. Liu, J. Pan, et al., Biomimetic composite scaffold of hydroxyapatite/gelatin-chitosan core-shell nanofibers for bone tissue engineering, Mater. Sci. Eng. C Mater. Biol. Appl. 97 (2019) 325–335.
[23] Y. Gong, P. Wang, R. Cao, et al., Exudate absorbing and antimicrobial hydrogel integrated with multifunctional curcumin-loaded magnesium polyphenol network for facilitating burn wound healing, ACS Nano 17 (22) (2023) 22355–22370.
[24] D. Nie, P. Wang, C. Zang, et al., Preparation of ZnO-incorporated porous carbon nanofibers and adsorption performance investigation on methylene blue, ACS Omega 7 (2) (2022) 2198–2204.
[25] K. Mariia, M. Arif, J. Shi, et al., Novel chitosan-ulvan hydrogel reinforcement by cellulose nanocrystals with epidermal growth factor for enhanced wound healing: in vitro and in vivo analysis, Int. J. Biol. Macromol. 183 (2021) 435–446.
[26] H. Yu, Y. Li, Y. Pan, et al., Multifunctional porous poly (L-lactic acid) nanofiber membranes with enhanced anti-inflammation, angiogenesis and antibacterial properties for diabetic wound healin, J Nanobiotechnology. 21 (1) (2023) 110.
[27] H. Zhao, Y. Liu, Neutrophil extracellular traps induce fibroblast ferroptosis via IRE1α/XBP1-mediated ER stress to impair diabetic wound healing, Free Radic. Biol. Med. 236 (2025) 17–27.
[28] X. Zhang, H. Li, Y. Liu, et al., Acid-responsive CST@NPs enhanced diabetic wound healing through rescuing mitochondrial dysfunction, Bioact. Mater. 44 (2024) 269–282.
[29] J. Liu, S. Chen, Z. Zhang, et al., The oxidized hyaluronic acid hydrogels containing paeoniflorin microspheres regulates the polarization of M1/M2 macrophages to promote wound healing, Int. J. Biol. Macromol. 282 (Pt 5) (2024) 137107.
[30] L. Deng, C. Du, P. Song, et al., The role of oxidative stress and antioxidants in diabetic wound healing, Oxidative Med. Cell. Longev. 2021 (2021) 8852759.
[31] M.J. Malone-povolny, S.E. Maloney, M.H. Schoenfisch, Nitric oxide therapy for diabetic wound healing, Adv. Healthc. Mater. 8 (12) (2019) e1801210.
[32] G. Li, C.N. Ko, D. Li, et al., A small molecule HIF-1α stabilizer that accelerates diabetic wound healing, Nat. Commun. 12 (1) (2021) 3363.
[33] H. Zhang, J. Ming, H. Zhang, S. Fang, et al., A comprehensive review: advances in mesenchymal stem cell applications for burn wound repair, Stem Cells Int. 2025 (2025) 6683745.
[34] C. Liu, C. Cheng, K. Cheng, et al., Precision exosome engineering for enhanced wound healing and scar revision, J. Transl. Med. 23 (1) (2025) 578.
[35] D. Sieńko, I. Szabłowska-Gadomska, A. Nowak-Szwed, et al., The potential of mesenchymal stem/stromal cells in diabetic wounds and future directions for research and therapy-is it time for use in everyday practice? Int. J. Mol. Sci. 25 (22) (2024) 12171.
[36] T. Luo, P. Zhu, S. Li, et al., DFO-loaded PDA nanoparticles facilitated 3D stem cell spheroids for diabetic wound repair by normalizing the pathological microenvironment, Mater Today Bio. 33 (2025) 101973.
[37] Y. Li, D. Li, L. You, et al., Dcas9-based PDGFR-β activation ADSCs accelerate wound healing in diabetic mice through angiogenesis and ECM remodeling, Int. J. Mol. Sci. 24 (6) (2023) 5949.
[38] H. Feng, S. Gong, J. Liu, et al., Adipose-derived stem cell exosomes: mechanisms and therapeutic potentials in wound healing, Biomark. Res. 13 (1) (2025) 88.
[39] L. Dong, X. Li, W. Leng, et al., Adipose stem cells in tissue regeneration and repair: from bench to bedside, Regen Ther. 24 (2023) 547–560.
[40] V.A. Solarte David, V.R. Güiza-Argüello, M.L. Arango-Rodríguez, C.L. Sossa, S. M. Becerra-Bayona, Decellularized tissues for wound healing: towards closing the gap between scaffold design and effective extracellular matrix remodeling, front Bioeng Biotechnol. 10 (2022) 821852.
[41] J.Y. Ding, M.J. Chen, L.F. Wu, et al., Mesenchymal stem cell-derived extracellular vesicles in skin wound healing: roles, opportunities and challenges, Mil. Med. Res. 10 (1) (2023) 36.
[42] D. Sivaraj, K. Chen, A. Chattopadhyay, et al., Hydrogel scaffolds to deliver cell therapies for wound healing, Front. Bioeng. Biotechnol. 9 (2021) 660145.
[43] A. Ghasempour, H. Dehghan, M. Mahmoudi, F. Lavi Arab, Biomimetic scaffolds loaded with mesenchymal stem cells (MSCs) or MSC-derived exosomes for enhanced wound healing, Stem Cell Res Ther 15 (1) (2024) 406.
[44] A.H. Aghayan, D. Mohammadi, A. Atashi, Z. Jamalpoor, Synergistic effects of mesenchymal stem cells and their secretomes with scaffolds in burn wound healing: a systematic review and meta-analysis of preclinical studies, J. Transl. Med. 23 (1) (2025) 708.
[45] T. Zhang, W. Ping, M. Suo, et al., Stimuli-responsive hydrogels potentiating Photothermal therapy against Cancer stem cell-induced breast Cancer metastasis, ACS Nano 24 (2024).
[46] W.M. Facchinatto, D.M.D. Santos, A.L. Bukzem, et al., Insight into morphological, physicochemical and spectroscopic properties of β-chitin nanocrystalline structures, Carbohydr. Polym. 273 (2021) 118563.
[47] R. Jayakumar, V.V.D. Rani, K.T. Shalumon, et al., Bioactive and osteoblast cell attachment studies of novel alpha- and beta-chitin membranes for tissue-engineering applications, Int. J. Biol. Macromol. 45 (3) (2009) 260–264.
[48] Y. Zhao, S. Song, X. Ren, et al., Supramolecular adhesive hydrogels for tissue engineering applications, Chem. Rev. 122 (6) (2022) 5604–5640.
[49] W. Zhu, Y.J. Chuah, D.A. Wang, Bioadhesives for internal medical applications: a review, Acta Biomater. 74 (2018) 1–16.
[50] N.T. Nguyen, L.V. Nguyen, N.M. Tran, et al., The effect of oxidation degree and volume ratio of components on properties and applications of in situ cross-linking hydrogels based on chitosan and hyaluronic acid, Mater. Sci. Eng. C Mater. Biol. Appl. 103 (2019) 109670.
[51] J. Liu, S. Chen, Y. Liu, Z. Luo, et al., The oxidized hyaluronic acid hydrogels containing paeoniflorin microspheres regulates the polarization of M1/M2 macrophages to promote wound healing, Int. J. Biol. Macromol. 282 (Pt 5) (2024) 137107.
[52] S. Wang, T. Liang, C. Zhang, The relationship between expression level and gene polymorphism of inflammatory factors and sepsis risk, Sci. Rep. 15 (1) (2025) 6701.
[53] A. Al-Roub, N. Akhter, F. Al-Rashed, et al., TNFα induces matrix metalloproteinase-9 expression in monocytic cells through ACSL1/JNK/ERK/NF-kB signaling pathways, Sci. Rep. 13 (1) (2023) 14351.
[54] F. D. Benedetti, G, Prencipe, C. Bracaglia, et al., Targeting interferon-γ in hyperinflammation: opportunities and challenges, Nat. Rev. Rheumatol. 17 (11) (2021) 678–691.
[55] J.A. Woznicki, N. Saini, P. Flood, et al., TNF-α synergises with IFN-γ to induce caspase-8-JAK1/2-STAT1-dependent death of intestinal epithelial cells, Cell Death Dis. 12 (10) (2021) 864.
[56] W. Li, Q. Liu, J. Shi, X. Xu, J. Xu, The role of TNF-α in the fate regulation and functional reprogramming of mesenchymal stem cells in an inflammatory microenvironment, Front. Immunol. 14 (2023) 1074863.
[57] L. López-García, M.E. Castro-Manrreza, TNF-α and IFN-γ participate in improving the Immunoregulatory capacity of mesenchymal stem/stromal cells: importance of cell-cell contact and extracellular vesicles, Int. J. Mol. Sci. 22 (17) (2021) 9531.
[58] Y. An, B.T. Xu, S. R. Wan, et al., The role of oxidative stress in diabetes mellitus-induced vascular endothelial dysfunction, Cardiovasc. Diabetol. 22 (1) (2023) 237.1.
[59] Z. Hou, Y. Wang, S. Chen, Z. Luo, Y. Liu, Licochalcone a loaded multifunctional chitosan hyaluronic acid hydrogel with antibacterial and inflammatory regulating effects to promote wound healing, Int. J. Biol. Macromol. 283 (Pt 1) (2024) 137458.
[60] B.K. Shook, R.R. Wasko, G.C. Rivera-Gonzalez, et al., Myofibroblast proliferation and heterogeneity are supported by macrophages during skin repair, Science 362 (6417) (2018) eaar2971.
[61] M. Sharifiaghdam, E. Shaabani, R. Faridi-Majidi, S.C. De Smedt, K. Braeckmans, J. C. Fraire, Macrophages as a therapeutic target to promote diabetic wound healing, Mol. Ther. 30 (9) (2022) 2891–2908.
[62] M. Bagheri, M. Validi, A. Gholipour, P. Makvandi, E. Sharifi, Chitosan nanofiber biocomposites for potential wound healing applications: antioxidant activity with synergic antibacterial effect, Bioeng Transl Med. 7 (1) (2021) e10254.
[63] A. Bravo-nuevo, H. Sugimoto, S. Iyer, et al., RhoB loss prevents streptozotocin-induced diabetes and ameliorates diabetic complications in mice, Am. J. Pathol. 178 (1) (2011) 245–252.
[64] A. Leguina-ruzzi, R. Ortiz, V. Velarde, The streptozotocin-high fat diet induced diabetic mouse model exhibits severe skin damage and alterations in local lipid mediators, Biom. J. 41 (5) (2018) 328–332, Biom. J.
[65] O.A. Peña, P. Martin, Cellular and molecular mechanisms of skin wound healing, Nat. Rev. Mol. Cell Biol. 25 (8) (2024) 599–616.
[66] Y. Ning, Z. Yuan, Q. Wang, et al., Epigallocatechin-3-gallate promotes wound healing response in diabetic mice by activating keratinocytes and promoting re-epithelialization, Phytother. Res. 38 (2) (2024) 1013–1027.
[67] L. Qiang, S. Yang, Y. Cui, et al., Keratinocyte autophagy enables the activation of keratinocytes and fibroblastsand facilitates wound healing, Autophagy 17 (9) (2021) 2128–2143.
[68] H. Huang, L. Liang, D. Sun, et al., Rab37 promotes endothelial differentiation and accelerates ADSC-mediated diabetic wound healing through regulating secretion of Hsp90α and TIMP1, Stem Cell Rev. Rep. 19 (4) (2023) 1019–1033.
[69] V. Prabhu, B.S.S. Rao, A.C.K. Rao, K. Prasad, K.K. Mahato, Photobiomodulation invigorating collagen deposition, proliferating cell nuclear antigen and Ki67 expression during dermal wound repair in mice, Lasers Med. Sci. 37 (1) (2022) 171–180.
[70] Y. Guan, H. Niu, Z. Liu, et al., Sustained oxygenation accelerates diabetic wound healing by promoting epithelialization and angiogenesis and decreasing inflammation, Sci. Adv. 7 (35) (2021) eabj0153.
[71] Y. Fang, Y. Zhu, M. Zhang, et al., TLQP-21 facilitates diabetic wound healing by inducing angiogenesis through alleviating high glucose-induced injuries on endothelial progenitor cells, Naunyn Schmiedeberg's Arch. Pharmacol. 397 (7) (2024) 4993–5004.
[72] G. Arderiu, E. Peña, R. Aledo, et al., MicroRNA-145 regulates the differentiation of adipose stem cells toward microvascular endothelial cells and promotes angiogenesis, Circ. Res. 125 (1) (2019) 74–89.
[73] F. Yu, N. Witman, D. Yan, et al., Human adipose-derived stem cells enriched with VEGF-modified mRNA promote angiogenesis and long-term graft survival in a fat graft transplantation model, Stem Cell Res Ther 11 (1) (2020) 490.
[74] J.M. Brandner, S. Zacheja, P. Houdek, et al., Expression of matrix metalloproteinases, cytokines, and connexins in diabetic and nondiabetic human keratinocytes before and after transplantation into an ex vivo wound-healing model, Diabetes Care 31 (1) (2008) 114–120.
[75] J. Kan, Y. Hui, W. Xie, et al., Lily bulbs' polyphenols extract ameliorates oxidative stress and lipid accumulation in vitro and in vivo, J. Sci. Food Agric. 101 (12) (2021) 5038–5048.
[76] Z. Fan, X. Chen, T. Liu, et al., Pectin oligosaccharides improved lipid metabolism in white adipose tissue of high-fat diet fed mice, Food Sci. Biotechnol. 31 (9) (2022) 1197–1205.

[77] L.S. Chow, S. Li, L.E. Eberly, et al., Estimated plasma stearoyl co-a desaturase-1 activity and risk of incident diabetes: the atherosclerosis risk in communities (ARIC) study, Metabolism 62 (1) (2013) 100–108.
[78] S. Vilarinho, S. Sari, F. MAzzacuva, et al., ACOX2 deficiency: a disorder of bile acid synthesis with transaminase elevation, liver fibrosis, ataxia, and cognitive impairment, Proc. Natl. Acad. Sci. USA 113 (40) (2016) 11289–11293.
[79] Y. Xiong, S. Knoedler, M. Alfertshofer, et al., Mechanisms and therapeutic opportunities in metabolic aberrations of diabetic wounds: a narrative review, Cell Death Dis. 16 (1) (2025) 341.
[80] C.C. Chang, M.S. Hsieh, S.T. Liao, Y.H. Chen, C.W. Cheng, P.T. Huang, Y.F. Lin, C. H. Chen, Hyaluronan regulates PPARγ and inflammatory responses in IL-1β-stimulated human chondrosarcoma cells, a model for osteoarthritis, Carbohydr. Polym. 90 (2) (2012) 1168–1175.
[81] K. Gharib-Naseri, S. de Las Heras-Saldana, S. Kheravii, L. Qin, J. Wang, S.B. Wu, Necrotic enteritis challenge regulates peroxisome proliferator-1 activated receptors signaling and β-oxidation pathways in broiler chickens, Anim Nutr. 7 (1) (2021) 239–251.
[82] M. Alonso, A. Serrano, M. Vida, A. Crespillo, L. Hernandez-Folgado, et al., Anti-obesity efficacy of LH-21, a cannabinoid CB(1) receptor antagonist with poor brain penetration, in diet-induced obese rats, Br. J. Pharmacol. 165 (7) (2012) 2274–2291.
[83] N. Mahmoudi, S. Sharifi, D. Leshchiner, et al., Tailored bioengineering and nanomedicine strategies for sex-specific healing of chronic wounds, Br. J. Dermatol. 192 (3) (2025) 390–401.
[84] G.S. Ashcroft, J.J. Ashworth, Potential role of estrogens in wound healing, Am. J. Clin. Dermatol. 4 (11) (2003) 737–743.
[85] B.M. Steiner, A.M. Benvie, D. Lee, Y. Jiang, D.C. Berry, Cxcr4 regulates a pool of adipocyte progenitors and contributes to adiposity in a sex-dependent manner, Nat. Commun. 15 (1) (2024) 6622.
[86] H.J. Park, J.M. Choi, Sex-specific regulation of immune responses by PPARs, Exp. Mol. Med. 49 (8) (2017) e364.